Embolic stroke can occur as a complication of these procedures [1, 2] and is strongly associated with vulnerable carotid plaques consisting primarily of lipid-necrotic core and/or intraplaque hemorrhage accompanied by a thin fibrous cap [3, 4]. Thus, assessment of intraplaque characteristics and prediction of unstable plaques may be crucial for minimizing perisurgical embolic stroke events. Magnetic resonance (MR) plaque imaging is widely used for this purpose, but findings of the vulnerable plaques vary among articles particularly those based on T1-weighted (T1W) imaging, which is considered to be the most useful [5]. This can be attributed to marked inter-institutional differences in imaging techniques, i.e., spin echo (SE), cardiac-gated black-blood (BB) fast SE (FSE), magnetization-prepared rapid acquisition with gradient echo (MPRAGE), source image (SI) of three-dimensional (3D) time-of-flight (TOF) MR angiography (MRA) (SI-MRA), and others [4, 6–9], as well as a lack of cross-validation among these imaging techniques. Therefore, we directly compared four kinds of T1W imaging techniques and histopathological findings in patients with carotid stenosis to elucidate which technique can most accurately predict intraplaque components.

Methods

Patients

From August 2010 to November 2011, 31 consecutive patients (30 men, one woman; age range, 54–80 years; mean age, 69.6 years) with unilateral cervical carotid stenosis who underwent CEA were prospectively examined. Twenty-five carotid stenoses were symptomatic, and 18 were on the right side. In addition, severity of the stenoses was 70–99% (mean, 87.7%) based on North American Symptomatic Carotid Endarterectomy Trial (NASCET) criteria using digital subtraction angiography. Clinical characteristics of the patients included hypertension in 22 patients, hyperlipidemia in 18, and diabetes mellitus in 14. The following drugs were administered to the patients: antiplatelet agents in 31 patients, angiotensin-2 receptor blocker in 13, statin in 13, and insulin in two. All examinations in this study were performed after obtaining approval from the institutional review board and a written informed consent from each patient.

Imaging protocol

Four kinds of axial T1W images of the affected carotid bifurcation were obtained within 1 week prior to CEA using a 1.5-T MR scanner (Echelon Vega, Hitachi Medical Corporation, Tokyo, Japan) and an eight-channel neurovascular coil. The following imaging techniques and pulse sequence parameters were used: (1) non-gated SE; repetition time (TR), 500 ms; echo time (TE), 12 ms; field of view (FOV), 18 cm; matrix size, 256×256 (pixel size, 0.35×0.35 mm after zero-fill interpolation); slice thickness, 4.0 mm with interslice gaps of 1 mm; number of slices, 9; number of excitations, 2; chemical shift selective saturation (CHESS) pulse for fat suppression; non-selective saturation pulse for blood signal suppression; self-navigated radial scan adapted from periodically rotated overlapping parallel lines with enhanced reconstruction method [10] for motion correction; and acquisition time, 6 min 46 s; (2) cardiac-gated BB-FSE; TR, 1 cardiac cycle (800–1,250 ms; median, 1,000 ms) for motion correction; TE, 12 ms; FOV, 18 cm; matrix size, 256×256; slice thickness, 4.0 mm with interslice gaps of 1 mm; number of slices, 1; CHESS pulse for fat signal suppression; double inversion recovery (IR) preparatory pulses for blood signal suppression; and acquisition time, 1 min 47 s to 3 min 13 s; (3) IR-prepared fast gradient echo (GRE) that is equivalent to MPRAGE originally introduced as direct thrombus imaging [9]; TR, 1,500 ms; TE, 5.0 ms; inversion time (TI); 660 ms for blood signal suppression; FOV, 18 cm; matrix size, 256×204; slice thickness, 2.5 mm; number of slices, 35; water excitation for fat suppression; and acquisition time, 7 min; and (4) SI-MRA; spoiled GRE, TR, 35 ms; TE, 4.4 ms; flip angle 30°; FOV, 18 cm; matrix size, 256×256; slice thickness, 2.5 mm; number of slices, 30; CHESS pulse for fat signal suppression; and acquisition time, 4 min 21 s. The section direction was carefully set as perpendicular to the long axis of carotid bifurcation on the sagittal two-dimensional phase-contrast MR angiography (2D-PC MRA), the section of BB-FSE was set at the location in which the stenosis was most severe, and the mid-sections of non-gated SE, MPRAGE, and SI-MRA were set at the identical location as that of BB-FSE.

Histological evaluation

Specimens excised from the carotid bifurcations in an en bloc fashion by one of the authors (K.O.) during CEA were provided for histological evaluation. After fixation by formaldehyde, transverse sections of the carotid bifurcations with the direction and position corresponding to those of the MR images were carefully obtained by one of the authors (J.H.) on referring to the MR images including 2D-PC-MRA in which the location of the section was indicated. Histological slices of decalcified and paraffin-embedded 7-μm-thick sections were stained by hematoxylin–eosin (HE), Masson-trichrome (MT), and antiglycophorin-A (AGP) methods.

Data and statistical analyses

For quantitative evaluation of MR imaging, the signal intensities of the carotid plaque and the adjacent sternomastoid muscle were measured at the section at which four

kinds of images were obtained. The regions of interest were manually traced three times with intervals of 3–5 days on a liquid crystal display (LCD) using the polygon cursor of a free software package (zioTerm2009, Ziosoft, Tokyo, Japan) by one of the authors (A.S.) who was blinded to the clinical and MR findings. The obtained signal intensity values were then averaged, and the contrast ratio (CR) of the carotid plaque was calculated by dividing the plaque signal intensity with the muscle signal intensity.

For quantitative assessment of the histological specimens, areas of the three components within the plaque, i.e., fibrous tissue, lipid/necrosis, or hemorrhage, were microscopically measured three times with intervals of 3–5 days using a manual tracing method and a free software package (ImageJ Ver. 1.44, National Institute of Health, Bethesda) by one of the authors (S.N.) who was blinded to the clinical and MR findings. Based on the averaged values of these measurements, the principal component of each plaque was determined when the area of one of the components was 50% or more of the total plaque area.

For statistical analyses, the Friedman test and the post hoc Wilcoxon test were used to determine differences in CRs of the carotid plaques among the four kinds of images obtained with different scanning methods. Kruskal–Wallis test and post-hoc Mann–Whitney test were used to determine differences among the three kinds of plaques with different main components. To determine the sensitivity and specificity of the images for the prediction of main intraplaque components, receiver operating characteristic (ROC) analyses were also performed. Furthermore, intraoperator agreements in quantitative measurements were assessed by calculating the intraclass correlation coefficient (ICC). The alpha level used was 0.05.

Results

Among 31 patients, three patients were excluded because of poor image quality due to remarkable motion artifacts, seven patients were excluded because no intraplaque component reached 50% of the total plaque area by the histological measurements, and the remaining 21 patients (54–80 years; mean age, 69.0 years) were subjects for further analyses. The measurements on histological specimens in these patients showed that the main component of the plaques was fibrous tissue in five cases (range, 53–95%; median, 66%), lipid/necrosis in six cases (50–81%; 58%), and hemorrhage in ten cases (50–66%; 58%).

CRs of the carotid plaques to the adjacent muscles were 0.92–2.30 (median, 1.52), 0.89–1.42 (1.13), 0.77–2.43 (1.42), and 1.01–2.57 (1.39) on the images with non-gated SE, BB-FSE, MPRAGE, and SI-MRA, respectively ($p<0.001$, Friedman test), and showed significant differences between BB-FSE and other methods ($p<0.001$ and $p=0.02$, post-hoc Wilcoxon test) as well as between MPRAGE and SI-MRA ($p=0.03$, post-hoc Wilcoxon test) (Fig. 1). CRs of the carotid plaques mainly containing fibrous tissue, lipid/necrosis, and hemorrhage based on non-gated SE were 0.92–1.15 (1.02), 1.22–1.52 (1.35), and 1.55–2.30 (1.81), respectively, and showed significant differences among these groups ($p<0.001$, Kruskal–Wallis test), as well as, between any combinations among these (fibrous-lipid/necrosis, $p=0.004$; fibrous-hemorrhage, $p=0.001$, lipid/necrosis-hemorrhage, $p<0.001$; Mann–Whitney test) (Table 1, Figs. 1, 2, 3 and 4). However, CRs of the plaques based on BB-FSE were 0.89–1.10 (1.09), 1.07–1.23 (1.10), and 1.01–1.42 (1.27), respectively, and showed less significant differences with larger overlaps ($p=0.01$, Kruskal–Wallis test; fibrous-lipid/necrosis, $p=0.33$; fibrous-hemorrhage, $p=0.008$, lipid/necrosis-hemorrhage, $p=0.03$; Mann–Whitney test) compared with CRs based on other imaging techniques (Table 1, Figs. 1, 2, 3 and 4). Furthermore, CRs of the plaques based on MPRAGE were 0.77–1.07 (0.91), 0.85–1.42 (1.10), and 1.45–2.43 (1.83), respectively; insignificant difference with a substantial overlap between the plaques with fibrous tissue and those with lipid/necrosis ($p=0.08$, Mann–Whitney test) was observed, although marked significant differences were found between the other two combinations (fibrous-hemorrhage, $p<0.001$; lipid/necrosis-hemorrhage, $p<0.001$; Mann–Whitney test) (Table 1, Figs. 1, 2, 3 and 4). SI-MRA showed similar results to MPRAGE: 1.01–1.39 (1.07), 1.12–1.39 (1.29), and 1.45–2.57 (1.87), respectively ($p<0.001$, Kruskal–Wallis test; fibrous-lipid/necrosis, $p=0.13$; fibrous-hemorrhage, $p=0.001$, lipid/necrosis-hemorrhage, $p<0.001$; Mann–Whitney test) (Figs. 1, 2, 3 and 4).

ROC analyses showed that the sensitivities and specificities for discriminating the plaques consisting mainly of lipid/necrosis or hemorrhage, from those consisting mainly of fibrous tissue, were 100% and 100% on non-gated SE with a cut off value of 1.19, 75% and 100% on cardiac-gated BB-FSE with a cut-off value of 1.11, 88% and 100% on MPRAGE with a cut off value of 1.08, and 100% and 80% on SI-MRA with a cut off value of 1.10, respectively. The ICC values for the measurements on MR images and histological specimens were 0.98–0.99 (median, 0.99) and 0.95–0.99 (median, 0.98), respectively, indicating excellent intraoperator agreements between the measurements obtained in this study.

Discussion

Several previous studies have compared findings from T1W MR plaque imaging with those from specimens obtained by CEA. In these studies, hyperintensity in the plaques tended

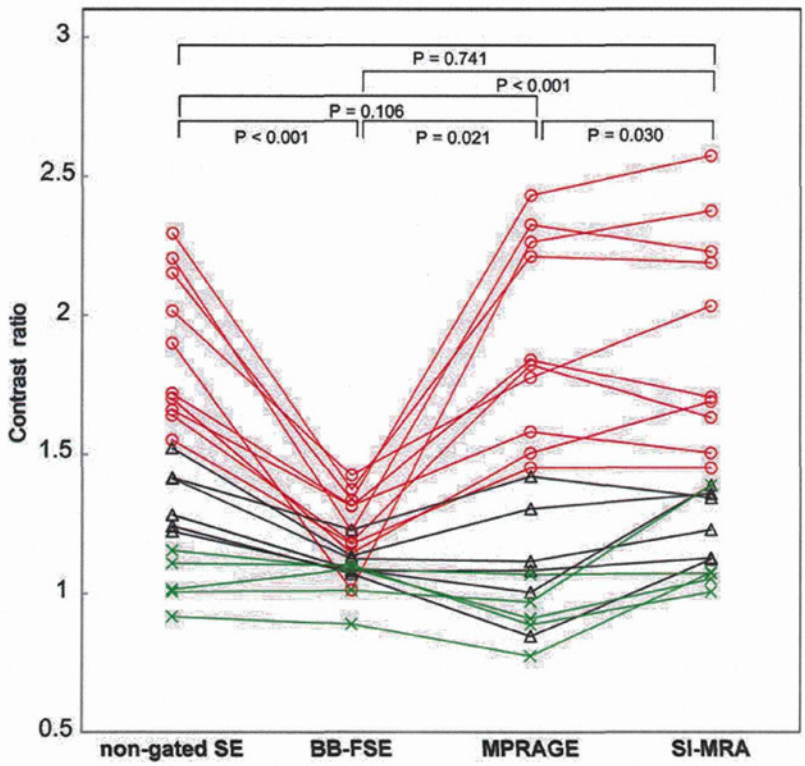

Fig. 1 Contrast ratios of the carotid plaques on T1-weighted images obtained through different imaging techniques. *SE* spin echo, *BB-FSE* black-blood fast spin echo, *MPRAGE* magnetization-prepared rapid acquisition with gradient echo, *SI-MRA* source image of three-dimensional time-of-flight MR angiography; *red lines* indicate plaques consisting mainly of hemorrhagic component, *black lines* indicate plaques consisting mainly of lipid/necrotic component, *green lines* indicate plaques consisting mainly of fibrous component; p values: Wilcoxon test. Contrast ratios (*CRs*) of the plaques to the adjacent muscles based on non-gated SE images are markedly different with little overlaps among plaques with different main components. However, CRs of the plaques based on BB-FSE are less different with marked overlaps among the groups. CRs of the plaques based on MPRAGE and SI-MRA consisting mainly of lipid/necrosis tend to overlap with those of fibrous tissue

to reflect a lipid-rich necrotic core and/or intraplaque hemorrhage, whereas isointensity to the adjacent muscle tended to reflect fibrous tissue [6–8, 11–13]. However, sensitivities and specificities for detecting vulnerable plaque components varied markedly among the studies: 56–96% and 84–94%, respectively [8, 9, 14]. In the present study, we showed substantial differences in the intraplaque contrast among different T1W plaque imaging techniques and indicated that non-gated SE is superior to BB-FSE, MPRAGE, and SI-MRA for discrimination of main intraplaque components. These results suggest that the variance in the previous studies can be attributed in part to differences in the imaging techniques used.

The cardiac-gated BB-FSE method appears to be the most popular technique for MR plaque imaging; however, in the present study, intraplaque contrast using this method

Table 1 Contrast ratios of the carotid plaque on various T1-weighted imaging techniques

	Main plaque component			Kruskal–Wallis Test (*p* values)	Mann–Whitney test (*p* values)		
	Fibrous tissue (*n*=5)	Lipid/necrosis (*n*=6)	Hemorrhage (*n*=10)		Fibrous vs. lipid/necrosis	Fibrous vs. hemorrhage	Lipid/necrosis vs. hemorrhage
Non-gated SE	0.92–1.15 (1.02)	1.22–1.52 (1.35)	1.55–2.30 (1.81)	<0.001	0.004	0.001	<0.001
Gated BB-FSE	0.89–1.10 (1.09)	1.07–1.23 (1.10)	1.01–1.42 (1.27)	0.011	0.329	0.008	0.031
MPRAGE	0.77–1.07 (0.91)	0.85–1.42 (1.10)	1.45–2.43 (1.83)	<0.001	0.082	0.001	<0.001
SI-MRA	1.01–1.39 (1.07)	1.12–1.39 (1.29)	1.45–2.57 (1.87)	<0.001	0.126	0.001	<0.001

BB-FSE black-blood fast spin–echo, *MPRAGE* magnetization-prepared rapid acquisition with gradient echo, *SE* spin–echo, *SI-MRA* source image of three-dimensional time-of-flight magnetic resonance angiography. Data are presented as range (median)

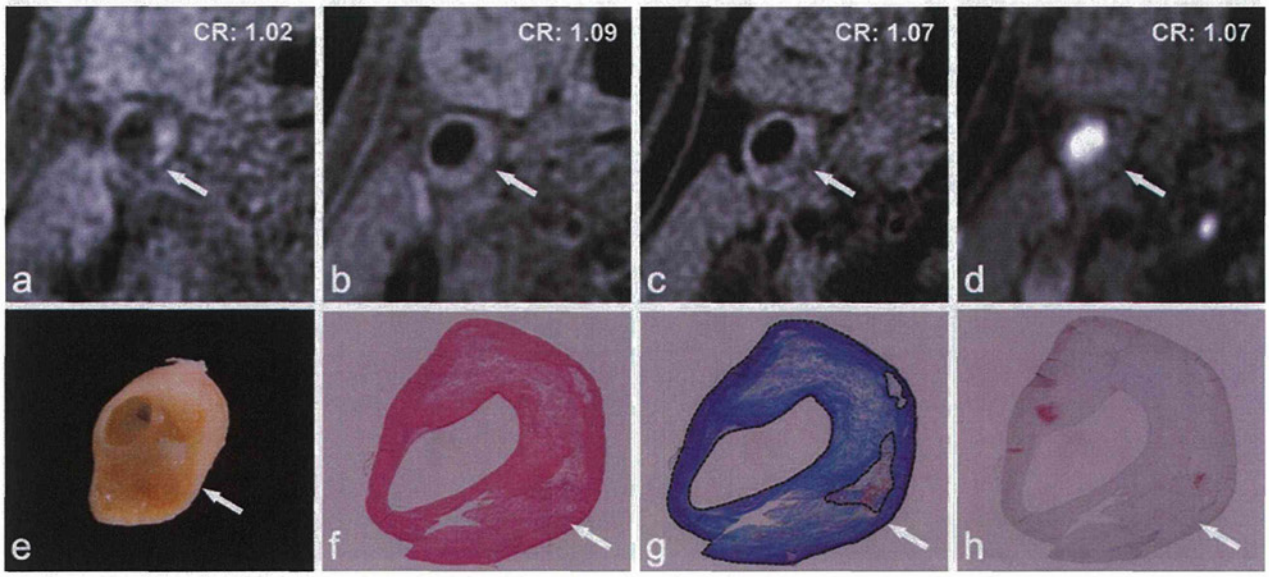

Fig. 2 T1-weighted MR images obtained by different techniques and corresponding pathological findings of the carotid plaque containing mainly fibrous tissue (75-year-old man with right carotid stenosis). **a** Non-gated SE; **b** BB-FSE; **c** MPRAGE; **d** SI-MRA; **e** macroscopic specimen; **f, g, h** histological specimens with hematoxylin–eosin, Masson-trichrome, and antiglycophorin-A staining methods, respectively. *CR* contrast ratio. On all MR images, the plaque shows near isointensity to the adjacent muscle (a–d, arrows). On macroscopic and microscopic specimens, the plaque consists mainly of fibrous tissue (delineated by *dotted lines*, 90% of the entire plaque area) (e–g, *arrows*)

was less conspicuous than that of the other methods. Using BB-FSE, TR is forced to depend on a one R–R interval, resulting in a TR of 800–1,000 ms, which is too long to diminish proton-density weighted contrast and to enhance T1W contrast [11]. Thus, inappropriately long TR can deteriorate the contrast originating from lipid and hemorrhagic

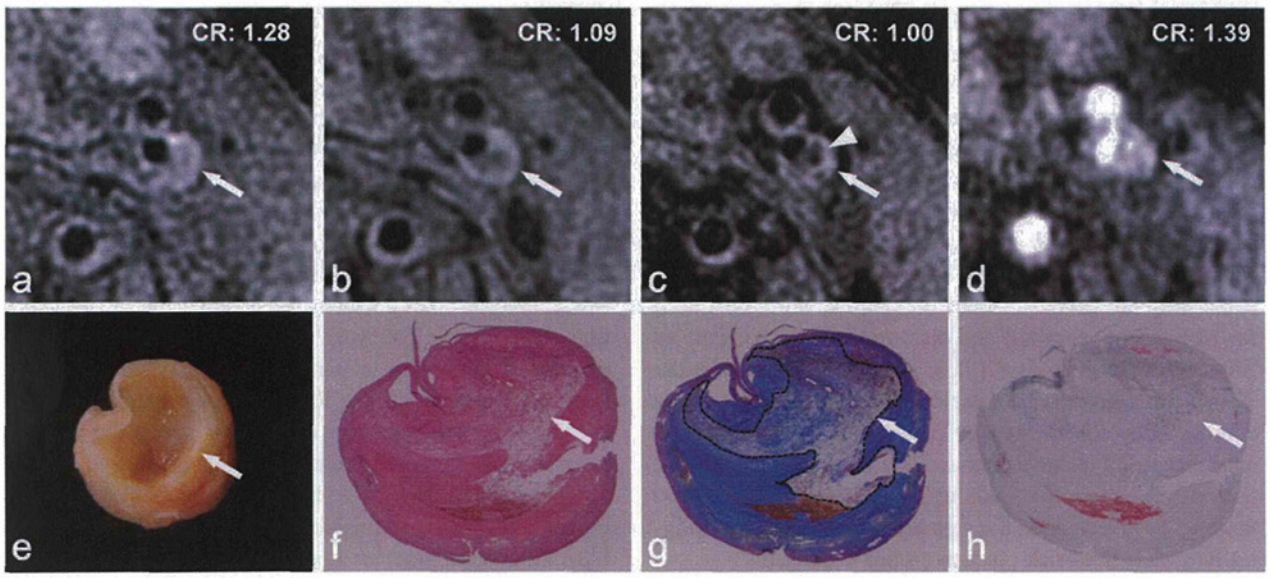

Fig. 3 T1-weighted MR images obtained by different techniques and corresponding pathological findings of the carotid plaque containing mainly lipid and necrosis (71-year-old man with left carotid stenosis). **a** Non-gated SE; **b** BB-FSE; **c** MPRAGE; **d** SI-MRA; **e** macroscopic specimen; **f, g, h** histological specimens with hematoxylin–eosin, Masson-trichrome, and antiglycophorin-A staining methods, respectively. *CR* contrast ratio. The plaque shows moderate hyperintensity on non-gated SE and SI-MRA images, but almost isointensity on BB-FSE and MP-RAGE (**a–d**, *arrows*). In addition, a part of the plaque shows hypointensity on MPRAGE (c, *arrowhead*). Pathological specimens show that the plaque consists of lipid/necrotic component (delineated by *dotted lines*, 52% of the entire plaque area) (e–h, *arrows*)

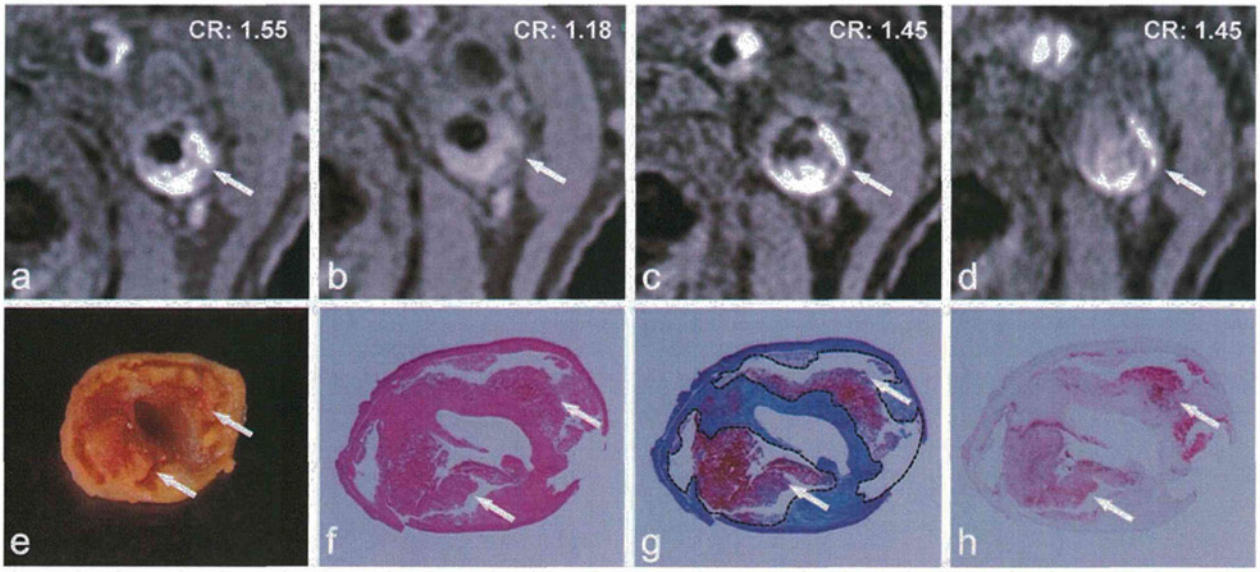

Fig. 4 T1-weighted MR images obtained by different techniques and corresponding pathological findings of the carotid plaque containing mainly hemorrhage (73-year-old man with left carotid stenosis). **a** Non-gated SE, **b** BB-FSE, **c** MPRAGE, **d** SI-MRA, **e** macroscopic specimen; **f**, **g**, **h** histological specimens with hematoxylin–eosin, Masson-trichrome, and antiglycophorin-A staining methods, respectively. *CR* contrast ratio. The plaque shows evident hyperintensity on non-gated SE, MPRAGE, and SI-MRA images (**a**, **c**, **d**; *arrows*), but mild hyperintensity on BB-FSE (**b**, *arrow*). A low signal spot at the anterior margin of the plaque may indicate small calcification. Pathological specimens show that the plaque contains massive hemorrhage (delineated by *dotted lines*, 53% of the entire plaque area) (**e**–**g**, *arrows*)

components within the plaques, which appears to be an inherent disadvantage of this technique. Besides the cardiac gating, proton-density weighted contrast is known to be substantially preserved on T1W spoiled GRE techniques that are generally used for MRA; this feature could result in an insufficient contrast between the fibrous and lipid/necrotic plaques on SI-MRA in this study.

In the present study, we indicated that MPRAGE could readily distinguish the plaques consisting mainly of intraplaque hemorrhage that showed marked hyperintensity, as reported in previous studies [4, 9, 15]. However, our results indicated that the lipid-rich plaques sometimes showed iso- or hypointensity on MPRAGE and could not be discriminated from the fibrous plaques. In general, MPRAGE used for MR plaque imaging, and was originally introduced as "direct thrombus imaging" [9], is a modified sequence as the TI is set at a null point of the blood to enable black-blood effects. Thus, signal intensity of the lipid/necrotic component that tends to have similar T1 values to blood can be theoretically attenuated, although no previous studies have thoroughly investigated the signal changes in the pathologically proven lipid-rich plaques on this sequence.

We showed that non-gated SE, which is a classical standard sequence, showed excellent intraplaque contrast and could discriminate plaques with different components better than BB-FSE, MPRAGE, and SI-MRA. These results can be explained by the fact that this can avoid substantial influences of the proton density and inversion recovery pulse. Non-gated SE needs a relatively long acquisition time, and is relatively susceptible to patient motions even when using a motion correction technique; however, this method is widely applicable in any scanners, can be used for assessing intraplaque characteristics and changes in patients with mild carotid stenosis who are not candidates for CEA or CAS [16], and may be used for multicenter trials.

Although, the present study has provided new insights into which kinds of MR imaging techniques are better for discriminating intraplaque characteristics, this study also has several limitations which must be taken into account when interpreting the results. First, direct comparisons were made between 2D (non-gated SE and BB-FSE) and 3D (MPRAGE and SI-MRA) images, among which slice thickness and image location could not be precisely matched. This could result in substantial errors due to partial volume effects during the quantitative measurements. Relatively low spatial resolution in these images due to usage of the 1.5-T scanner and neurovascular coil could also cause partial volume effects. In addition, measurements were performed on only a single section because multi-slice acquisition was not available using the BB-FSE method. Furthermore, although histological sections were carefully prepared, locations of MR images were not matched perfectly to those of the histology specimens. These issues may decrease the reliability and reproducibility of the results in this study to some extent.

Another limitation of this study is that signal intensity of the entire plaque was measured by a manual tracing

technique to calculate the CR. Intraplaque components are usually heterogeneous so that CRs in this study reflect a mixture of fibrous, lipid/necrotic, and hemorrhagic components with various percentages. Presence of calcification, which was occasionally observed in the plaques, also can affect the CR values; we did not assess this in this study because T1W images we used poorly visualize the calcific component. Further, plaques containing massive hemorrhagic or lipid/necrotic components with a thin fibrous cap can be unstable, even if the principal component is fibrous tissue and/or calcification. Manual tracing also can affect reproducibility of the measurements among the different images and sessions. For more precise comparisons among MR images and histopathological images, including assessment of the thickness of the fibrous cap, sub-regional measurements or measurements on a pixel-by-pixel basis are required.

In addition, this study could not accurately determine sensitivity and specificity of the four kinds of imaging techniques for discriminating plaques that consist mainly of lipid/necrosis and/or hemorrhage from plaques that consist mainly of fibrous tissue. This is due to the relatively small number of patients involved in the study, which included only five cases of fibrous plaques. Further investigation with a larger sample size is necessary to confirm our results. This study also did not clarify whether novel 3D-FSE techniques [17, 18] have sufficient contrast as compared with the classical techniques, whether addition of other images, such as T2-weighted images, can contribute to further discrimination of the intraplaque components [19], whether visual interpretation can accurately characterize the plaques as compared with signal measurements, or whether differences in the static magnetic field affect intraplaque contrast because there are substantial differences in signal-to-noise, spatial resolution, T1 relaxation, and susceptibility effects between 1.5 and 3 T [20]. These parameters, although beyond the scope of this manuscript, should also be investigated further.

In conclusion, contrast of T1W MR plaque imaging significantly varied among the four kinds of imaging techniques examined here. Importantly, images obtained using non-gated SE method can more accurately characterize main intraplaque components in patients who underwent CEA when compared with other imaging techniques, such as cardiac-gated BB-FSE, MPRAGE, and SI-MRA methods.

Acknowledgements This work was supported in part by a Research Grant for Cardiovascular Diseases (20C-1) from the Ministry of Heath, Labor and Welfare of Japan, a Grant-in-Aid for Strategic Medical Science Research Center, and Grants-in-Aid for Science Research (22890169, 22590963) from the Ministry of Education, Culture, Sports, Science and Technology of Japan.

Conflict of interest MS consults for Hitachi Medical Corporation and has received honoraria for lectures from the same company.

References

1. Brott TG, Hobson RW 2nd, Howard G, Roubin GS, Clark WM, Brooks W, Mackey A, Hill MD, Leimgruber PP, Sheffet AJ, Howard VJ, Moore WS, Voeks JH, Hopkins LN, Cutlip DE, Cohen DJ, Popma JJ, Ferguson RD, Cohen SN, Blackshear JL, Silver FL, Mohr JP, Lal BK, Meschia JF (2010) Stenting versus endarterectomy for treatment of carotid-artery stenosis. N Engl J Med 363:11–23
2. Yamada K, Yoshimura S, Kawasaki M, Enomoto Y, Asano T, Hara A, Minatoguchi S, Iwama T (2011) Embolic complications after carotid artery stenting or carotid endarterectomy are associated with tissue characteristics of carotid plaques evaluated by magnetic resonance imaging. Atherosclerosis 215:399–404
3. Takaya N, Yuan C, Chu B, Saam T, Underhill H, Cai J, Tran N, Polissar NL, Isaac C, Ferguson MS, Garden GA, Cramer SC, Maravilla KR, Hashimoto B, Hatsukami TS (2006) Association between carotid plaque characteristics and subsequent ischemic cerebrovascular events: a prospective assessment with MRI—initial results. Stroke 37:818–823
4. Yamada N, Higashi M, Otsubo R, Sakuma T, Oyama N, Tanaka R, Iihara K, Naritomi H, Minematsu K, Naito H (2007) Association between signal hyperintensity on T1-weighted MR imaging of carotid plaques and ipsilateral ischemic events. AJNR Am J Neuroradiol 28:287–292
5. Hatsukami TS, Yuan C (2010) MRI in the early identification and classification of high-risk atherosclerotic carotid plaques. Imaging Med 2:63–75
6. Yoshida K, Narumi O, Chin M, Inoue K, Tabuchi T, Oda K, Nagayama M, Egawa N, Hojo M, Goto Y, Watanabe Y, Yamagata S (2008) Characterization of carotid atherosclerosis and detection of soft plaque with use of black-blood MR imaging. AJNR Am J Neuroradiol 29:868–874
7. Yoshimura S, Yamada K, Kawasaki M, Asano T, Kanematsu M, Takamatsu M, Hara A (2011) High-intensity signal on time-of-flight magnetic resonance angiography indicates carotid plaques at high risk for cerebral embolism during stenting. Stroke 42:3132–3137
8. Watanabe Y, Nagayama M, Suga T, Yoshida K, Yamagata S, Okumura A, Amoh Y, Nakashita S, Van Cauteren M, Dodo Y (2008) Characterization of atherosclerotic plaque of carotid arteries with histopathological correlation: vascular wall MR imaging vs. color Doppler ultrasonography (US). J Magn Reson Imaging 28:478–485
9. Moody AR, Murphy RE, Morgan PS, Martel AL, Delay GS, Allder S, MacSweeney ST, Tennant WG, Gladman J, Lowe J, Hunt BJ (2003) Characterization of complicated carotid plaque with magnetic resonance direct thrombus imaging in patients with cerebral ischemia. Circulation 107:3047–3052
10. Tamhane AA, Arfanakis K (2009) Motion correction in periodically-rotated overlapping parallel lines with enhanced reconstruction (PROPELLER) and turboprop MRI. Magn Reson Med 62:174–182
11. Narumi S, Sasaki M, Ohba H, Ogasawara K, Hitomi J, Mori K, Ohura K, Ono A, Terayama Y (2010) Altered carotid plaque signal among different repetition times on T1-weighted magnetic resonance plaque imaging with self-navigated radial-scan technique. Neuroradiology 52:285–290
12. Yuan C, Mitsumori LM, Beach KW, Maravilla KR (2001) Carotid atherosclerotic plaque: noninvasive MR characterization and identification of vulnerable lesions. Radiology 221:285–299

13. Chu B, Kampschulte A, Ferguson MS, Kerwin WS, Yarnykh VL, O'Brien KD, Polissar NL, Hatsukami TS, Yuan C (2004) Hemorrhage in the atherosclerotic carotid plaque: a high-resolution MRI study. Stroke 35:1079–1084
14. Ota H, Yarnykh VL, Ferguson MS, Underhill HR, Demarco JK, Zhu DC, Oikawa M, Dong L, Zhao X, Collar A, Hatsukami TS, Yuan C (2010) Carotid intraplaque hemorrhage imaging at 3.0-T MR imaging: comparison of the diagnostic performance of three T1-weighted sequences. Radiology 254:551–563
15. Hishikawa T, Iihara K, Yamada N, Ishibashi-Ueda H, Miyamoto S (2010) Assessment of necrotic core with intraplaque hemorrhage in atherosclerotic carotid artery plaque by MR imaging with 3D gradient–echo sequence in patients with high-grade stenosis. Clinical article. J Neurosurg 113:890–896
16. Yamaguchi M, Sasaki M, Ohba H, Mori K, Narumi S, Katsura N, Ohura K, Kudo K, Terayama Y (2012) Quantitative assessment of changes in carotid plaques during cilostazol administration using three-dimensional ultrasonography and non-gated magnetic resonance plaque imaging. Neuroradiology [Epub ahead of print]
17. Balu N, Chu B, Hatsukami TS, Yuan C, Yarnykh VL (2008) Comparison between 2D and 3D high-resolution black-blood techniques for carotid artery wall imaging in clinically significant atherosclerosis. J Magn Reson Imaging 27:918–924
18. Crowe LA, Gatehouse P, Yang GZ, Mohiaddin RH, Varghese A, Charrier C, Keegan J, Firmin DN (2003) Volume-selective 3D turbo spin echo imaging for vascular wall imaging and distensibility measurement. J Magn Reson Imaging 17:572–580
19. Cappendijk VC, Heeneman S, Kessels AG, Cleutjens KB, Schurink GW, Welten RJ, Mess WH, van Suylen RJ, Leiner T, Daemen MJ, van Engelshoven JM, Kooi ME (2008) Comparison of single-sequence T1w TFE MRI with multisequence MRI for the quantification of lipid-rich necrotic core in atherosclerotic plaque. J Magn Reson Imaging 27:1347–1355
20. Underhill HR, Yarnykh VL, Hatsukami TS, Wang J, Balu N, Hayes CE, Oikawa M, Yu W, Xu D, Chu B, Wyman BT, Polissar NL, Yuan C (2008) Carotid plaque morphology and composition: initial comparison between 1.5- and 3.0-T magnetic field strengths. Radiology 248:550–560

Histochem Cell Biol
DOI 10.1007/s00418-013-1082-0

ORIGINAL PAPER

Effects of protease-activated receptors (PARs) on intracellular calcium dynamics of acinar cells in rat lacrimal glands

Makoto Oikawa · Tomoyuki Saino · Katsura Kimura · Yuki Kamada · Yasunori Tamagawa · Daijiro Kurosaka · Yoh-ichi Satoh

Accepted: 4 February 2013

Abstract Protease-activated receptors (PARs) represent a novel class of seven transmembrane domain G-protein coupled receptors, which are activated by proteolytic cleavage. PARs are present in a variety of cells and have been prominently implicated in the regulation of a number of vital functions. Here, lacrimal gland acinar cell responses to PAR activation were examined, with special reference to intracellular Ca^{2+} concentration ($[Ca^{2+}]_i$) dynamics. In the present study, detection of acinar cell mRNA specific to known PAR subtypes was determined by reverse transcriptase polymerase chain reaction. Only PAR2 mRNA was detected in acinar cells of lacrimal glands. Both trypsin and a PAR2-activating peptide (PAR2-AP), SLIGRL-NH_2, induced an increase in $[Ca^{2+}]_i$ in acinar cells. The removal of extracellular Ca^{2+} and the use of Ca^{2+} channel blockers did not inhibit PAR2-AP-induced $[Ca^{2+}]_i$ increases. Furthermore, U73122 and xestospongin C failed to inhibit PAR2-induced increases in $[Ca^{2+}]_i$. The origin of the calcium influx observed after activated PAR2-induced Ca^{2+} release from intracellular Ca^{2+} stores was also evaluated. The NO donor, GEA 3162, mimicked the effects of PAR2 in activating non-capacitative calcium entry (NCCE). However, both calyculin A (100 nM) and a low concentration of Gd^{3+} (5 μM) did not completely block the PAR2-AP-induced increase in $[Ca^{2+}]_i$. These findings indicated that PAR2 activation resulted primarily in Ca^{2+} mobilization from intracellular Ca^{2+} stores and that PAR2-mediated $[Ca^{2+}]_i$ changes were mainly independent of IP_3. RT-PCR indicated that TRPC 1, 3 and 6, which play a role in CCE and NCCE, are expressed in acinar cells. We suggest that PAR2-AP differentially regulates both NCCE and CCE, predominantly NCCE. Finally, our results suggested that PAR2 may function as a key receptor in calcium-related cell homeostasis under pathophysiological conditions such as tissue injury or inflammation.

Keywords Lacrimal gland · Protease-activated receptors · Intracellular calcium · Confocal microscopy · RT-PCR

Introduction

The lacrimal gland is responsible for secretion of electrolytes, water, proteins and mucins, collectively known as lacrimal gland fluid, into the tear film. The appropriate amount and composition of lacrimal gland fluid is crucial for a healthy, intact ocular surface (Dartt 2009). Regulation of these secretions is under neural control, and activation of the sensory nerves in the cornea and conjunctiva initiates an afferent pathway leading to the central nervous system. This pathway activates an efferent pathway that stimulates parasympathetic and sympathetic nerves, innervating the lacrimal gland (Hodges and Dartt 2003).

Protease-activated receptors (PARs) represent a novel class of seven transmembrane domain G-protein coupled receptors (GPCRs) that are activated by proteolytic cleavage (Déry et al. 1998). Four members of this class of

M. Oikawa · T. Saino (✉) · Y. Tamagawa · Y. Satoh
Department of Anatomy (Cell Biology),
Iwate Medical University, 2-1-1 Nishitokuda,
Yahaba, Iwate 028-3694, Japan
e-mail: tsaino@iwate-med.ac.jp

K. Kimura (✉) · Y. Kamada · D. Kurosaka
Department of Ophthalmology, School of Medicine,
Iwate Medical University, 19-1 Uchimaru, Morioka,
Iwate 020-8505, Japan
e-mail: kimukatu@iwate-med.ac.jp

Published online: 06 March 2013

receptors have been identified: PAR1, -2, -3 and -4 (Vu et al. 1991; Nystedt et al. 1994; Ishihara et al. 1997; Kahn et al. 1998; Xu et al. 1998; Hollenberg 1999). The mechanism of PAR activation involves the proteolytic unmasking of an N-terminal sequence that acts as a tethered ligand (Déry et al. 1998). Thrombin functions as an agonist for PAR1, -3, and -4 (Vu et al. 1991; Ishihara et al. 1997; Kahn et al. 1998; Xu et al. 1998), and trypsin is a major agonist for PAR2 (Nystedt et al. 1994). In addition, mast cell tryptase, as well as coagulation factors VIIa and Xa, are generally thought to serve as significant agonists of PAR2 (Nystedt et al. 1994; Camerer et al. 2000; Kawabata and Kuroda 2000). Therefore, the activation of PAR in cells by various proteases plays an essential role in inflammation, pain, and other physiological and pathological responses (Nystedt et al. 1994; Kawabata et al. 1998, 2000a, b; Hollenberg 1999; Cocks and Moffatt 2000; Coughlin 2000; Macfarlane et al. 2001; Hirano and Kanaide 2003; Ossovskaya and Bunnett 2004).

PAR2 is involved in a variety of biological events in the alimentary, cardiovascular, respiratory, and central nervous systems and is abundantly expressed in the pancreas, as well as the parotid, sublingual, submandibular, and lacrimal glands (Böhm et al. 1996; Nguyen et al. 1999; Kawabata et al. 2000a, b; Nishikawa et al. 2005; Nishiyama et al. 2007). PAR2-activating peptides (PAR2-APs), administered systemically to mice or rats, trigger prompt salivation and tear secretion in vivo (Kawabata et al. 2000b, 2001; Nishikawa et al. 2005). In an in vitro study, PAR2-APs and the endogenous PAR2 activator trypsin were shown to induce the secretion of amylase and mucin from isolated rat parotid glands and sublingual glands, respectively (Kawabata et al. 2000a, b). In addition, PAR2-APs administered systemically cause a prompt increase followed by a transient decrease in secretion of pancreatic juice and subsequently produce persistent increased pancreatic juice secretion in anesthetized rats (Kawabata et al. 2000b). PAR2-APs facilitate secretion of amylase in isolated pancreatic acinar fragments in vitro (Böhm et al. 1996) and in conscious mice (Kawabata et al. 2002). These previous studies indicate that PAR2 plays a key role in the regulation of digestive exocrine secretion. However, few studies have investigated the relationship between PARs and intracellular Ca^{2+} concentration ($[Ca^{2+}]_i$). In addition, a previous study showed that inflammatory mediators function by activating specific receptors, many of which are GPCRs that use Gq or G11 types of Gα proteins for signaling and activate phospholipase C (PLC) (Linley et al. 2008), which cleaves membrane-bound phosphatidylinositol biphosphate to generate inositoltriphosphate (IP_3) and diacylglycerol; IP_3 causes Ca^{2+} mobilization from internal stores (Berridge 2009). PARs are GPCRs; thus, PARs should induce changes in $[Ca^{2+}]_i$, and such activation should be suppressed by inhibition of PLC or the IP_3 receptor. However, preliminary experiments using exocrine glandular cells showed that treatment with the PLC inhibitor U73122 did not suppress PAR2-mediated $[Ca^{2+}]_i$ changes.

In most cells, receptors that activate phospholipase C (PLC) stimulate both release of Ca^{2+} from intracellular stores and Ca^{2+} influx. The former is mediated by IP_3 receptors, and the latter is often thought to be mediated by capacitative Ca^{2+} entry (CCE), which is activated by depletion of intracellular Ca^{2+} stores (Putney et al. 2001). In addition to CCE, non-capacitative Ca^{2+} entry (NCCE) pathways regulated by a variety of intracellular signals may play an important role in secondary Ca^{2+} influx induced by activation of PLC-linked receptors in some cell types (Taylor 2002; Shuttleworth 2004). The transient receptor potential cation (TRPC) channels are mammalian homologs of the photoreceptor transient receptor potential (TRP) channel in *Drosophila melanogaster* (Montell 2003). The mammalian TRPC family can be divided into TRPC1/4/5 and TRPC3/6/7 subgroups based on sequence homology and functional properties (Birnbaumer et al. 2003). Results from a number of studies have supported the role of TRPC channels in both CCE and NCCE pathways (Vazquez et al. 2004; Cheng et al. 2008; Jardin et al. 2008; Liao et al. 2008).

The aim of this study was to determine whether acinar cells of the lacrimal glands expressed PARs and whether there was a relationship between PARs and $[Ca^{2+}]_i$. Reverse transcription polymerase chain reaction (RT-PCR) was used to examine PAR expression in intact rat lacrimal glands, which are composed of various types of cells. The signaling mechanism of PAR-induced $[Ca^{2+}]_i$ changes in lacrimal glands was also examined. Because the signaling mechanisms of primary cells may be altered upon culture, intact lacrimal glands were used for these studies. We also aimed to determine the IP_3-dependency of PAR2-mediated $[Ca^{2+}]_i$ changes in lacrimal glands. Further, we considered whether PAR2-induced Ca^{2+} influx might underlie the change in behavior of CCE and/or NCCE.

Materials and methods

Preparation of rat glandular acini

Protocols and all animal experiments were approved by and conducted under the authority of the Iwate Medical University Institutional Animal Care and Use Committee. Adult Wistar male rats (ages 7–12 weeks old, body weight 180–300 g) were used. The rats were killed using carbon dioxide gas and then perfused via the left cardiac ventricle with Ringer's solution (147 mM NaCl, 4 mM KCl, and 2.25 mM $CaCl_2$) at room temperature. The lacrimal glands

were removed and placed in Hepes-buffered Ringer's solution (HR) containing 118 mM NaCl, 4.7 mM KCl, 1.25 mM $CaCl_2$, 1.13 mM $MgCl_2$, 1 mM NaH_2PO_4, 5.5 mM D-glucose, MEM amino acids solution (Gibco, Grand Island, NY, USA), 0.2 % bovine serum albumin (Sigma, St. Louis, MO, USA), and 10 mM Hepes, and the pH was adjusted to 7.4 with NaOH.

Lacrimal glands from male rats were trimmed of excessive connective tissues and digested with collagenase (100 U/mL; Elastin Products, Owensville, MO) in HR buffer for 1 h at 37 °C. Enzyme digestion was conducted with constant agitation (~200 cycles/min) in a rotary shaker under an atmosphere of 100 % O_2 that was achieved by gassing at 15-min intervals. After digestion, the glands were washed twice and centrifuged at $800\times g$ for 2 min at room temperature between washes. The pellet was resuspended in 15 mL of HR buffer. The suspension was filtered through a Nitex screen (150 mesh/in.). The glands were then washed twice and centrifuged at $800\times g$ for 2 min at room temperature between washes. The final pellet was resuspended in 3 mL of HR buffer.

Intracellular Ca^{2+} imaging

The specimens were transferred into HR buffer containing 3 μM Indo-1/AM and 0.02 % Cremophore®-EL (Nacalai Tesque, Kyoto, Japan) and were incubated for 1 h at 37 °C. After incubation, in order to measure $[Ca^{2+}]_i$, lacrimal gland acinar cells were placed on coverslips coated with Cell-Tak® (a nontoxic adhesive reagent; Collaborative Biomedical, Bedford, MA, USA) in modified Sykus-Moore chambers and were then continuously perfused with HR buffer containing selected stimulants.

Indo-1, a ratiometric dye that is excited by ultraviolet light, was used for quantitative determination of $[Ca^{2+}]_i$. The emission maximum of Indo-1 shifts from 475 nm in Ca^{2+}-free medium to 400 nm when the dye solution is saturated with Ca^{2+}. The ratio of the emission intensity at a wavelength shorter than 440 nm to that at a wavelength longer than 440 nm was used to estimate $[Ca^{2+}]_i$; higher ratios indicated higher $[Ca^{2+}]_i$; ratiometry by one excitation-two emissions dye. One excitation-two emissions ratiometry is cut out for real-time changes of $[Ca^{2+}]_i$, compared with ratiometry using fura-2 which is two excitations-one emission fluorescent dye, in which time-lag for image acquisition is necessary. In addition, indo-1 tends to remain in the cytoplasm without compartmentalization, although photobleaching of indo-1 is relatively fast. In the present study, we would like to observe changes of each cell in acini. To this end, we used ratiometry with indo-1 under confocal laser scanning microscopy.

A real-time confocal microscope (RCM/Ab; a modified version of a Nikon model RCM-8000, Tokyo, Japan) was used. Acini, loaded with Indo-1, were exposed to an ultraviolet-beam (351 nm). An inverted microscope was equipped with an argon-ion laser (TE-300, Nikon), and the fluorescence emission was passed through a water-immersion objective lens (Nikon C Apo 40×, N.A. 1.15) to a pinhole diaphragm. Using this system, the acquisition time per image frame was 1/30 s. Images were immediately stored on high-speed hard disks. The digital images in the laser scanning microscopic imaging were composed of 512 × 480 pixels with a density resolution of 8 bits/pixel. Fluorescence intensities were displayed as pseudocolor with 256 colors; red represented high $[Ca^{2+}]_i$ and purple and blue represented low $[Ca^{2+}]_i$. We measured $[Ca^{2+}]_i$ changes in specific, restricted areas of the cell ($\sim 0.5\ \mu m^2$ spot sizes).

Perfusion

The $[Ca^{2+}]_i$ dynamics of acini were examined in a perfusion chamber as quickly as possible after the dye-loading procedure. After perfusion with the standard HR solution for a few minutes at room temperature, intact lacrimal glands were selected and examined under the microscope. Specimens were continuously perfused with the HR solution containing the following agonists and/or antagonists: thrombin derived from bovine plasma (2 U/mL; Sigma); trypsin derived from porcine pancreas (3,000 U/mL; Sigma); PAR2-AP, a synthetic agonist for PAR2-AP (SLIGRL-NH_2; 200 μM; American Peptide Company, Vista, USA); U73122 (5 μM; a specific inhibitor of phospholipase C; Sigma); diltiazem (50 μM; an L-type Ca^{2+} channel blocker; Sigma); Gd^{3+} (5 μM; a capacitative Ca^{2+} entry blocker; Sigma); xestospongin C (2 μM; a novel blocker of IP_3 receptor; Calbiochem, Darmstadt, Germany); calyculin A (100 nM; a capacitative Ca^{2+} entry blocker; Calbiochem); 2-aminoethoxydiphenyl borate (2-APB; 100 μM; an inhibitor of TRPC channels as well as a blocker of IP_3-dependent Ca^{2+} release; Tocris, Bristol, UK); GEA3162 (200 μM; a nitric oxide [NO] donor; Enzo Life Sciences, Ann Arbor, USA); and thapsigargin (2 μM, a microsomal Ca^{2+}-ATPase inhibitor; Sigma). Doses of proteases, PAR2-AP, and others used in the present study were determined by preliminary studies. Experiments in each group were performed at least 8 times.

Histology

Rats were killed using carbon dioxide gas. They were then perfused via the left ventricle with oxygenated standard HR solution for 5 min and then with standard HR or with HR containing PAR2-AP (200 μM) for 30 min. The animals were subsequently perfused with a fixative containing

1.25 % glutaraldehyde and 4 % paraformaldehyde in phosphate-buffered saline (PBS; 100 mM) for approximately 4 h at room temperature. Specimens were then postfixed in 1 % osmium tetroxide (Merck, Germany) in PBS for 1.5 h at 4 °C, dehydrated in a series of ethanol and embedded in Epon 812 (TAAB, Berkshire, UK). Semi-thin (~1-μm-thick) sections were consecutively cut using an ultramicrotome (2088 Ultrotome; LKB, Bromma, Sweden) and were stained with toluidine blue. The sections were examined by light microscopy.

RNA amplification and RT-PCR

Lacrimal glands from rats were digested with collagenase in HR buffer as described above. Total RNA was extracted from samples using the RNeasy Micro Kit (Qiagen, Hilden, Germany) according to the manufacturer's instructions. RNA concentrations were determined by spectroscopy at 260 nm. Isolated RNA was subjected to RT-PCR performed in a thermal cycler (PC-701, ASTEC, Fukuoka, Japan) using a ReverTra Ace-α-® kit (TOYOBO, Osaka, Japan). The primer sequences used to amplify PAR proteins are shown in Table 1 and were previously described by Rohatgi et al. (2003). The primer sequences used to amplify TRP cation channels (TRPCs) and cation channel subfamily V member 1 (TRPV1) are shown in Table 2 and were previously described by Matsuoka et al. (2009) and Yoo et al. (2012). The thermal cycling protocol was as follows: 42 °C for 10 min followed by 94 °C for 1 min, then 35 cycles of 94 °C for 45 s, 58 °C for 30 s, and 72 °C for 2 min, followed by 72 °C for 10 min. The PCR products were electrophoresed on 2 % agarose gels and were stained with ethidium bromide. Images of the gels were captured using a Polaroid MP4 Land Camera. Each RT-PCR was repeated in three independent experiments.

Depiction of peak value in $[Ca^{2+}]_i$ changes

From 4 to 6 measurements of the peak of ratio indicating $[Ca^{2+}]_i$ of ROIs in each chamber during PAR2-activation in various conditions (e.g., Figs. 3, 4, 5, 6, 7), the mean value was formed. For the depiction of the data obtained, the group mean values ± standard deviation (SD) were also calculated. To investigate the secondary Ca^{2+} entry mechanism, we also measured $[Ca^{2+}]_i$ values during extracellular Ca^{2+} re-introduction (e.g., Figs. 8, 9). The increase or inhibition was statistically verified by non-parametric *U*-test. The level of biological significance was set at $p \leq 0.05$.

Results

Histological changes in lacrimal glands following stimulation

The effects of PAR2-AP stimulation on the histology of rat lacrimal glands were analyzed using light microscopy. Control lacrimal gland acinar cells contained numerous

Table 1 Primers used for PCR analysis of protease activated receptor (PAR) expression

Receptor	Sequence 5′–3′	Position	Accession Code	Amplicon (bp)
PARI				
F	CCTATGAGACAGCCAGAATC	146	M81642	355
R	GCTTCTTGACCTTCATCC	500		
PAR2				
F	GCGTGGCTGCTGGGAGGTATC	19	U61373	742
R	GGAACAGAAAGACTCCAATG	760		
PAR3				
F	GTGTCTCTGCACACTTAGTG	18	AF310076	581
R	ATAGCACAATACATGTTGCC	598		
PAR4				
F	GGAATGCCAGACGCCCAGCATC	54	AF310216	559
R	GGTGAGGCGTTGACCACGCA	612		
GAPDH				
F	TTCAACGGCACAGTCAAGGC	1,009	AF106860	812
R	TCCACCACCCTGTTGCTGTAGC	1,820		

The primers listed are as described by Rohatgi et al. (2003). The run conditions are provided in the "Materials and methods"

F forward primer, *R* reverse primer. All primers were assessed for their sequence homology with other genes using BLAST searches (http://blast.ncbi.nlm.nih.gov/Blast.cgi)

Table 2 Primers used for the PCR analysis of TRPCs and TRPV1 expression

Receptor	Sequence 5′–3′	Position	Accession Code	Amplicon (bp)
TRPC1				
F	ATAACCAGAAGGAGTTTGTCTCCCAGTC	866	NM053558	367
R	TCTGACCAAATCATCCCAATAATCCACAG	1,232		
TRPC2				
F	CTGGTGGAACTTCCTGGACGTGGTC	2,913	XM002725704	317
R	GGATGAACATGAACCGGATCATGTCGTC	3,229		
TRPC3				
F	CAAGAAATCGAGGATGACAG	2,232	NM021771	322
R	GTCTTTTCATTATCTGCTGATA	2,553		
TRPC4				
F	CCGTCAAAAAGAGTTTGTTGC	888	NM001083115	498
R	GCACTGTACTTTACAAATGCGAC	1,385		
TRPC5				
F	GAACAACGCCTTCTCCACGCTCTTTGA	1,683	NM080898	471
R	CTGATAACTTCCTGATAATGTTG	2,153		
TRPC6				
F	ATACTACAATCTGGCCAGGATAAAGTG	1,728	NM053559	482
R	CATCATCCTCA ATTTC CTG G A ATG	2,209		
TRPC7				
F	ACTTCACCTACGCCAGGGA	1,662	NM001191691	475
R	TCCTCGATTTCCTGATAGGAG	2,136		
TRPV1				
F	GGGTCTGCCTGCAAGCCAGG	1,932	NM031982.1	463
R	TGCGCTTGACGCCCTCACAG	2,394		
GAPDH				
F	TTCAACGGCACAGTCAAGGC	1,009	AF106860	812
R	TCCACCACCCTGTTGCTGTAGC	1,820		

The primers listed are as described by Matsuoka et al. (2009) and Yoo et al. (2012), except for the TRPC2 reverse primer. The run conditions are provided in the "Materials and methods"

F forward primer, *R* reverse primer. All primers were assessed for their sequence homology with other genes using BLAST searches (http://blast.ncbi.nlm.nih.gov/Blast.cgi)

pale secretory granules and basally located nuclei. Acinar lumina were faintly detected under the light microscope (Fig. 1a). Exocytotic structures were rarely observed.

Following vascular perfusion with HR buffer containing PAR2-AP (200 μM), the lacrimal acini showed a wide lumen and conspicuous vacuolation (Fig. 1b). There were few microvilli on the exocytosing luminal surface. Contracted myoepithelial cells that were previously observed in guinea pig lacrimal glands (Satoh et al. 1994, 1997) were not evident in the rat lacrimal gland because of the relatively coarse net of the myoepithelial envelope.

Expression of PAR2 in rat lacrimal gland acinar cells

RT-PCR analysis of mRNA harvested from rat lacrimal glands yielded signals for PCR products of the predicted size for PARs (Table 1). Only PAR2 mRNA was detected in acinar cells of lacrimal gland (Fig. 2).

Effects of PAR2-AP on $[Ca^{2+}]_i$ dynamics

We next analyzed the effects of PAR2 on $[Ca^{2+}]_i$ dynamics in lacrimal gland acinar cells whose profiles could be clearly observed by confocal microscopy as shown in Fig. 2. Since we did not wish to include the myoepithelial cells that cover the acini in this microscopic study, we therefore set the focal plane on the equatorial planes of the acini, and placed the region of interest (ROI) on acinar cells for the time course of $[Ca^{2+}]_i$ dynamics. No spontaneous $[Ca^{2+}]_i$ changes were observed in the acinar cells of the lacrimal glands. The lacrimal gland specimens were then perfused with HR for 5 min before stimulation with selected reagents. Generally, damaged cells showed high

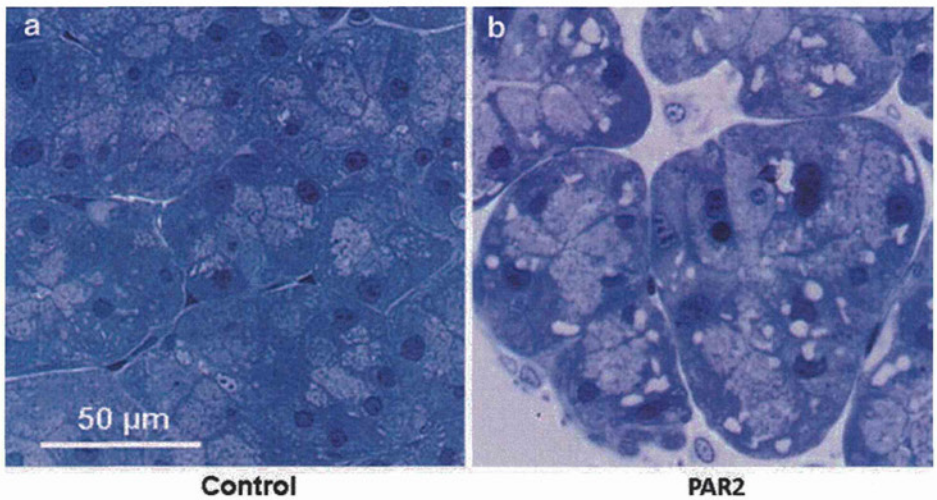

Fig. 1 Histological changes in lacrimal glands following stimulation. **a** Control, **b** PAR2-AP-stimulated glands. PAR2-AP caused exocytosis and also dilation of the lumen. Note the vacuolation, suggesting intracellular granule fusion. *Bar* 50 μm

Fig. 2 RT-PCR analysis of PAR mRNAs in rat lacrimal gland acinar cells. Amplified PAR mRNA fragments obtained using RT-PCR were analyzed by ethidium-bromide agarose gel electrophoresis. GAPDH was used as a positive control

$[Ca^{2+}]_i$. Therefore, lacrimal gland acinar cells that showed such high $[Ca^{2+}]_i$ under resting conditions were excluded from subsequent analyses. Ratios of basic resting conditions were about 0.5 in most acinar cells examined.

Thrombin, which activates PAR1, -3 and -4 (Vu et al. 1991; Ishihara et al. 1997; Kahn et al. 1998; Xu et al. 1998), failed to induce a $[Ca^{2+}]_i$ increase when used at 2 U/mL (Fig. 3a). Extracellular trypsin (3,000 U/mL), which activates PAR2, caused a transient increase in $[Ca^{2+}]_i$ in lacrimal gland acinar cells (Fig. 3b; mean and SD of peak ratio: 0.643 ± 0.032; number of ROIs of the specimen $n = 6$). Further study focused on elucidating the detailed mechanisms of PAR2-mediated responses.

Exposure of lacrimal glands to PAR2-AP led to an increase in $[Ca^{2+}]_i$ in some acinar cells (Fig. 4a–e; 0.678 ± 0.034; $n = 6$). At a tangential plane, myoepithelial cell profiles were sometimes observed, although the myoepithelial cell network of rat lacrimal gland acini was relatively coarse compared to that of guinea pig acini. Myoepithelial cells showed almost the same $[Ca^{2+}]_i$ changes during PAR2-AP stimulation (Fig. 5; acinar cells 0.677 ± 0.033; $n = 6$, myoepithelial cells 0.685 ± 0.034; $n = 5$).

To further analyze the mechanisms through which PAR2-AP induced changes in $[Ca^{2+}]_i$, we investigated the functions of ion channels. PAR2-AP-induced $[Ca^{2+}]_i$ changes in lacrimal gland acinar cells were not completely inhibited in the absence of extracellular Ca^{2+} ($[Ca^{2+}]_o$-free) (Fig. 6a; 0.657 ± 0.035; $n = 6$), although the inhibition was not statistically verified ($p = 0.18$). Treatment of acinar cells with diltiazem (50 μM), an L-type cation channel blocker, also did not completely inhibit PAR2-AP-induced $[Ca^{2+}]_i$ increases (Fig. 6b; 0.667 ± 0.013; $n = 9$) ($p = 0.31$). Furthermore, complete inhibition of PAR2-AP-induced $[Ca^{2+}]_i$ increases was also not observed following treatment with Gd^{3+} (100 μM), a nonspecific Ca^{2+} channel blocker (data not shown). These data suggested that receptors other than ion channels may also mediate the activity of PAR2.

Generally, metabotropic receptors are G-protein-linked, and stimulation of G proteins activates PLC, which cleaves membrane-bound phosphatidyl inositol biphosphate to generate IP_3 and diacylglycerol. This IP_3 subsequently causes Ca^{2+} mobilization from internal stores (Berridge 2009). To determine whether this mechanism of Ca^{2+} mobilization was involved in the observed PAR2-AP-dependent $[Ca^{2+}]_i$ increase, the effect of U73122, an inhibitor of PLC, was assayed. U73122 (5 μM) partially inhibited PAR2-AP-induced increases in $[Ca^{2+}]_i$ (Fig. 7a; 0.644 ± 0.031; $n = 6$). In addition, xestospongin C

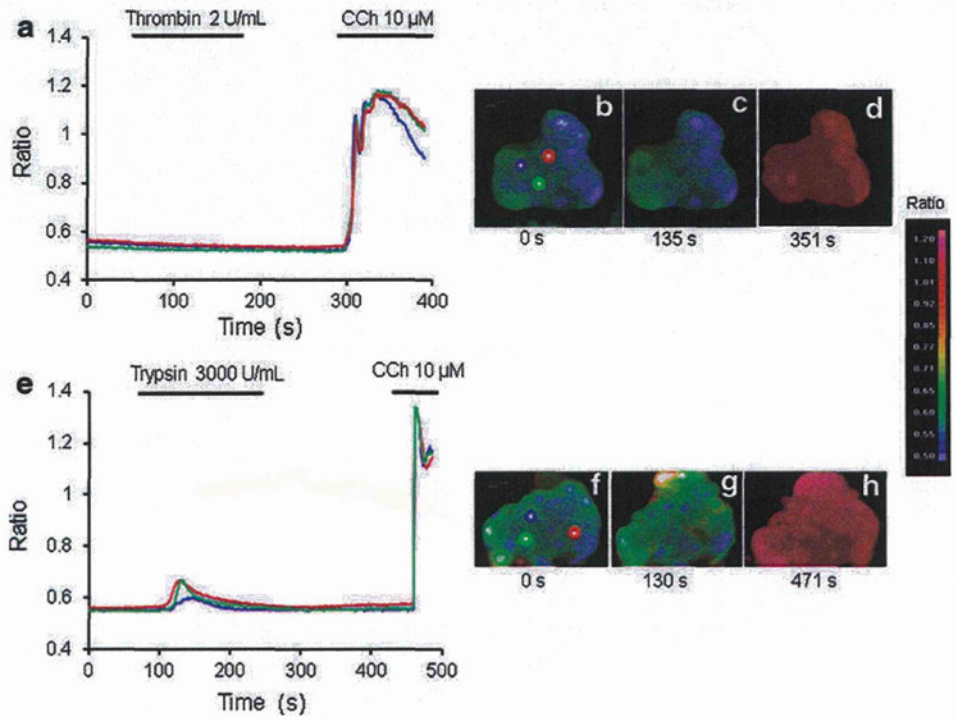

Fig. 3 Spatiotemporal changes of $[Ca^{2+}]_i$ in acinar cells during thrombin and trypsin stimulation. Changes in $[Ca^{2+}]_i$ are indicated as pseudocolors (**b–d** and **f–h**). *Color scale bar* $[Ca^{2+}]_i$ was calculated based on the ratio of dye fluorescence at different wavelengths. **a** The time course of thrombin-induced changes in $[Ca^{2+}]_i$ in specific areas (i.e., region of interest: ROI) of lacrimal gland acinar cells ($\sim 1\ \mu m^2$ in size) was analyzed. Thrombin failed to increase $[Ca^{2+}]_i$ in the cells. **e** The time course of trypsin-induced changes in $[Ca^{2+}]_i$ in specific areas of the cells was analyzed. Trypsin-induced $[Ca^{2+}]_i$ increases in lacrimal gland acinar cells were observed. Stimulation with carbachol (CCh: 10 μM) was used as a positive control

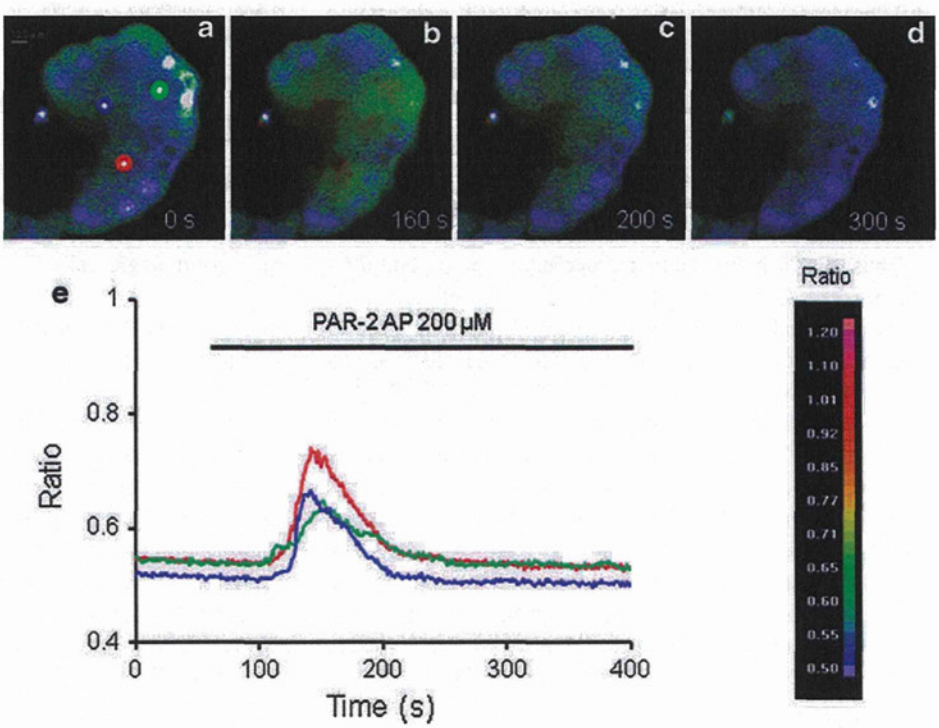

Fig. 4 Spatiotemporal changes of $[Ca^{2+}]_i$ in acinar cells during PAR2-AP stimulation. Changes in $[Ca^{2+}]_i$ are indicated as pseudocolors (**a–d**). *Color scale bar* $[Ca^{2+}]_i$ was calculated based on the ratio of dye fluorescence at different wavelengths. **e** The time course of PAR2-AP-induced changes in $[Ca^{2+}]_i$ in specific areas (i.e., region of interest: ROI) of lacrimal gland acinar cells ($\sim 1\ \mu m^2$ in size). Three ROIs were set

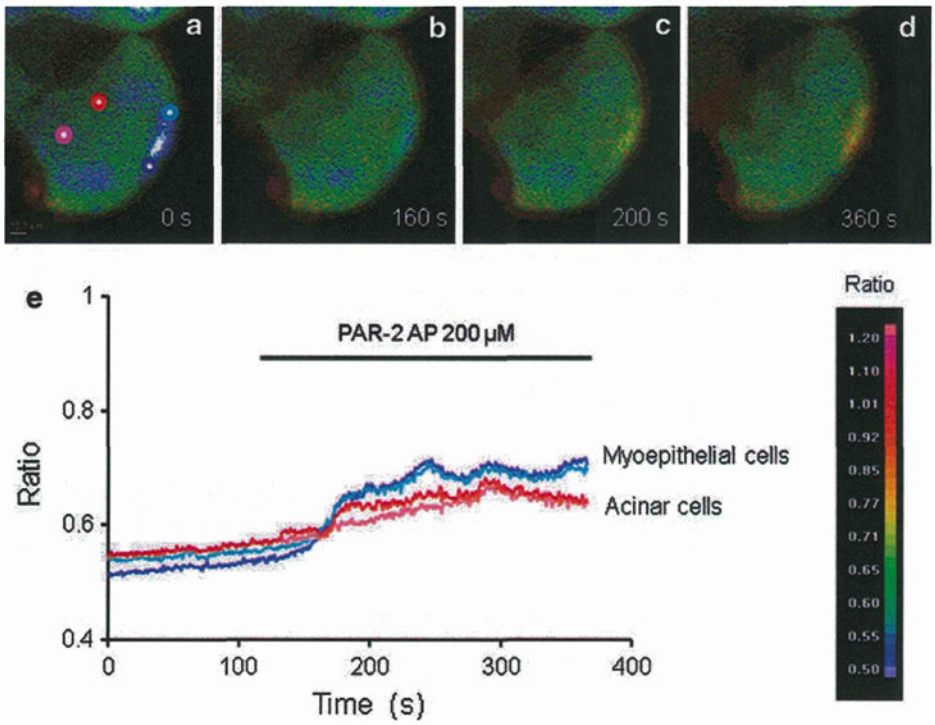

Fig. 5 Spatiotemporal changes of $[Ca^{2+}]_i$ changes in acinar cells and myoepithelial cells during PAR2-AP stimulation. Changes in $[Ca^{2+}]_i$ are indicated as pseudocolors (**a–d**). *Color scale bar* $[Ca^{2+}]_i$ was calculated based on the ratio of dye fluorescence at different wavelengths. **e** The time course of PAR2-AP-induced changes in $[Ca^{2+}]_i$ in specific areas (ROI) of lacrimal gland acinar cells (*red*, and *pink lines*)and myoepithelial cells (*blue*, and *sky blue lines*) (~1 μm^2 in size). Because of bright fluorescence and fusiform profiles, myoepithelial cells were clearly distinguishable from acinar cells

(2 μM) did not completely block these increases (Fig. 7b; 0.640 ± 0.013; $n = 6$). In both conditions, the inhibition was not statistically verified (U73122; $p = 0.48$, xestospongin C; $p = 0.700$). Since our results (Fig. 7a, b) indicated that PAR2-AP induced Ca^{2+} release from intracellular stores, further studies were conducted to determine whether thapsigargin and PAR2-AP caused the release of Ca^{2+} from the same pool. As shown in Fig. 7c, when acini were treated with thapsigargin (Tg; 2 μM) in nominally Ca^{2+}-free Hepes buffer, subsequent addition of PAR2-AP at 550 s failed to produce any further release, suggesting that both of these agents released Ca^{2+} from the same store.

Thus, Ca^{2+} influx from extracellular spaces and IP_3-independent Ca^{2+} mobilization from intracellular Ca^{2+} stores were induced by PAR2-AP stimulation, suggesting that mobilization of Ca^{2+} from intracellular Ca^{2+} stores may be more significant than Ca^{2+} influx in the PAR2-AP-induced response. Because PAR2 has been reported to increase $[Ca^{2+}]_i$ via IP_3-dependent Ca^{2+} mobilization in the dorsal motor nucleus of the vagus neurons of rats (DMV neuronal cells) (Wang et al. 2010), we next determined whether PAR2 activates Ca^{2+} entry via a CCE pathway by examining the effectiveness of the trivalent ion Gd^{3+} in blocking Ca^{2+} entry. Gadolinium has been reported to inhibit CCE at low concentrations without affecting the NCCE pathway (Broad et al. 1999). PAR2-AP induced Ca^{2+} entry (Fig. 8a; 0.669 ± 0.028; $n = 6$), however, the entry was slightly altered by the addition of 5 μM Gd^{3+} (Fig. 8b; 0.611 ± 0.031; $n = 6$). Addition of calyculin A (100 nM) prior to Ca^{2+} store-emptying also partially inhibited PAR2-AP-induced Ca^{2+} influx (Fig. 8c; 0.569 ± 0.014; $n = 8$). The inhibition was statistically verified ($p < 0.005$). PAR2-induced Ca^{2+} entry was almost completely blocked in the presence of 2-APB (Fig. 8d; 0.539 ± 0.013; $n = 7$). The inhibition was statistically verified ($p < 0.005$). Pretreatment of GEA 3162, PAR2-induced Ca^{2+} entry were significantly enhanced (Fig. 9; 0.88 ± 0.040; $n = 8$) ($p < 0.005$). A similar slow time course of NO-induced Ca^{2+} release was also observed in rat parotid single cells (Looms et al. 2001).

TRPC and TRPV1 receptor mRNA expression in lacrimal gland acinar cells

We finally assessed the expression of TRPC receptor mRNAs in lacrimal gland acinar cells using RT-PCR. Receptor expression levels were graded from (−), where the PCR product was not detectable by ethidium bromide staining of an agarose gel, to (+++), where a very strong band was detected in the gel (Fig. 10). Almost all TRPC receptor mRNAs that were investigated, i.e., TRPC1, -3, -6, and TRPV1 were expressed in the lacrimal gland acinar cells (Fig. 10; Table 2).

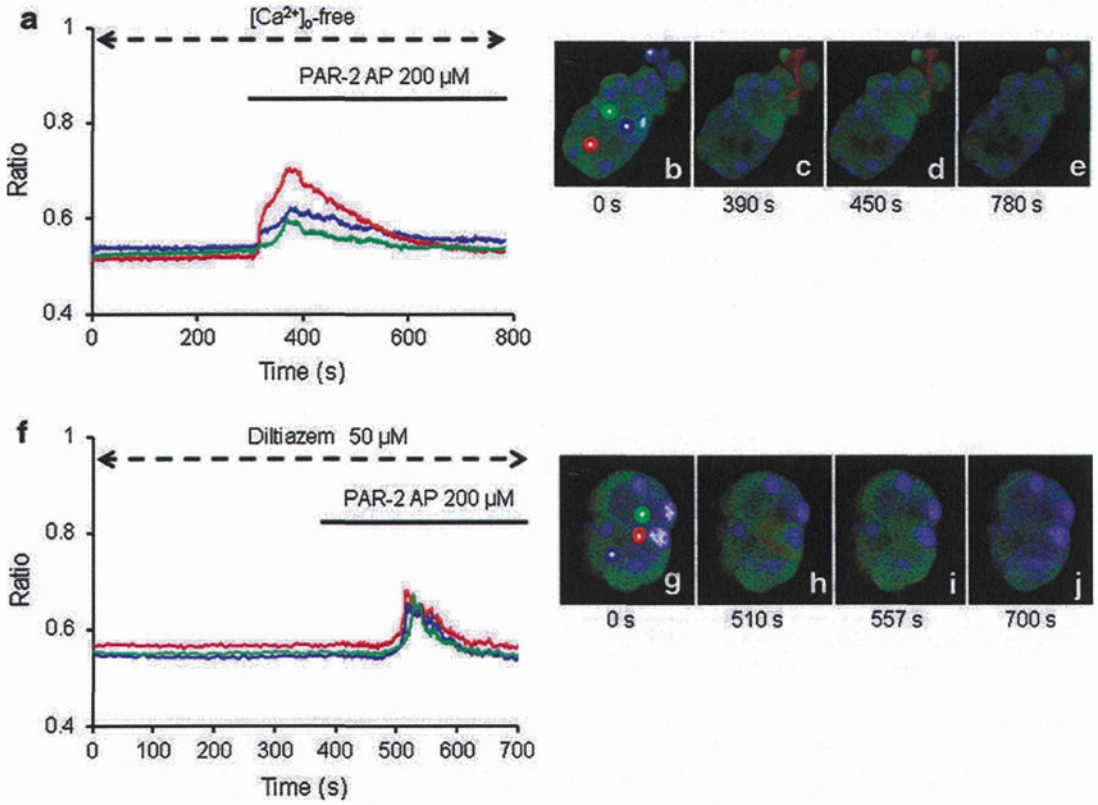

Fig. 6 Ion channels were not completely responsible for PAR2-AP-induced $[Ca^{2+}]_i$ changes. Changes in $[Ca^{2+}]_i$ are indicated as pseudocolors (**b–e** and **g–j**). Time course of $[Ca^{2+}]_i$ changes induced by PAR2-AP in specific areas of lacrimal gland acinar cells (~1 μm^2 in size). Neither extracellular Ca^{2+}-free conditions ($[Ca^{2+}]_o$-free) (**a**) nor treatment with 50 μM diltiazem (**f**) completely inhibited PAR2-AP-induced $[Ca^{2+}]_i$ increases. Three ROIs were set

Discussion

Various proteases play important roles in pathological conditions, such as inflammation and injury, and sympathetic nerves may be involved in tissue responses. However, few investigations of the potential role of PARs in lacrimal gland have been reported. The present study is the first investigation to demonstrate PAR expression in lacrimal glands, show that proteases induce $[Ca^{2+}]_i$ changes in both acinar and myoepithelial cells, and implicate proteases in lacrimal gland activation.

We previously observed that PAR2 activation induces a $[Ca^{2+}]_i$ increase in sympathetic nerves, indicating that blood vessel dilation may have been stimulated (Miura et al. 2011). It is conceivable that $[Ca^{2+}]_i$ changes stimulated by proteases in satellite cells are exclusively caused by Ca^{2+} mobilization from internal stores and are IP_3-independent, whereas Ca^{2+} influx and IP_3-dependent Ca^{2+} mobilization play an important role in neuron responses to proteases. Thus, although the responses of neurons and satellite cells were independent in this study, satellite cell activation by proteases may affect neuronal activity.

Lacrimal gland secretion is controlled by autonomic nerves. Parasympathetic cholinergic stimuli elicit an IP_3-dependent $[Ca^{2+}]_i$ increase, while sympathetic adrenergic stimulation-induced $[Ca^{2+}]_i$ dynamics are IP_3-independent (Dartt 1994; Gromada et al. 1995). We previously reported that acinar cells were stimulated by both cholinergic and adrenergic agonists, but that myoepithelial cells responded to only cholinergic stimuli (Satoh et al. 1997). Furthermore, we recently reported that Ca^{2+} mobilization from intracellular Ca^{2+} stores was induced by extracellular ATP, suggesting the presence of metabotropic receptors that are activated by ATP in rat lacrimal gland acinar cells (Kamada et al. 2012).

Therefore, even under conditions of increasing tension of the sympathetic nerve, the lacrimal gland can both secrete lacrimal gland fluid via an IP_3-dependent mechanism and excrete fluid via myoepithelial cell contraction. It is conceivable that different signaling pathways are necessary to ensure that the corneal surface is moist at all times. If lacrimation was competitively controlled by cholinergic and adrenergic nerves, it is possible that tear secretion may be stopped in certain cases, thereby resulting in drying of the cornea.

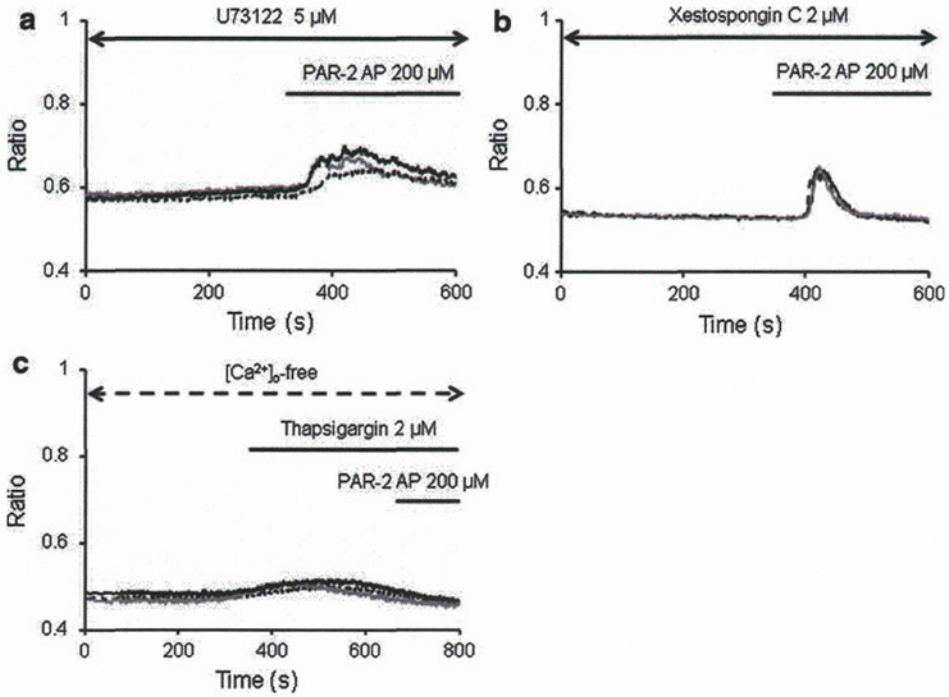

Fig. 7 A role for mobilization of Ca^{2+} from intracellular Ca^{2+} stores in PAR2-AP-induced $[Ca^{2+}]_i$ changes. PAR2-AP (200 µM) failed to inhibit a $[Ca^{2+}]_i$ increase in the cells after inhibition of phospholipase C by treatment with U73122 (5 µM) (**a**). Treatment with the IP_3 receptor antagonist, xestospongin C (2 µM) yielded similar results (**b**). Acini were incubated in nominally $[Ca^{2+}]_o$-free buffer 300 s prior to the addition of thapsigargin (2 µM), and PAR2-AP (200 µM) was added 640 s later (**c**). The temporal changes of $[Ca^{2+}]_i$ for three ROIs are depicted (*black*, *gray*, and *dotted lines*)

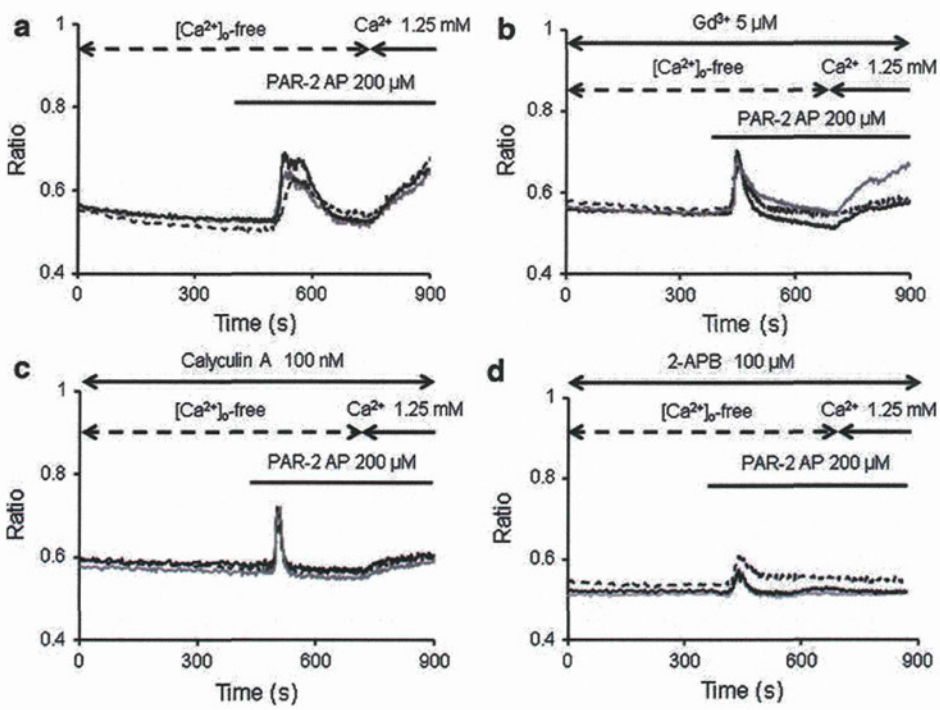

Fig. 8 Effects of Gd^{3+}, calyculin A or 2-APB on PAR2-AP induced Ca^{2+} release and Ca^{2+} entry in lacrimal gland acinar cells. Cells were incubated in nominally Ca^{2+}-free Hepes buffer ($[Ca^{2+}]_o$-free) in the absence (**a**) or presence (**b**) of Gd^{3+} (5 µM), 100 nM calyculin A (**c**), or 100 µM 2-APB (**d**) for 6 min, before the addition of PAR2-AP (200 µM). Ca^{2+} (1.25 mM) was reintroduced at 720 s. The temporal changes of $[Ca^{2+}]_i$ for three ROIs are depicted (*black*, *gray*, and *dotted lines*)

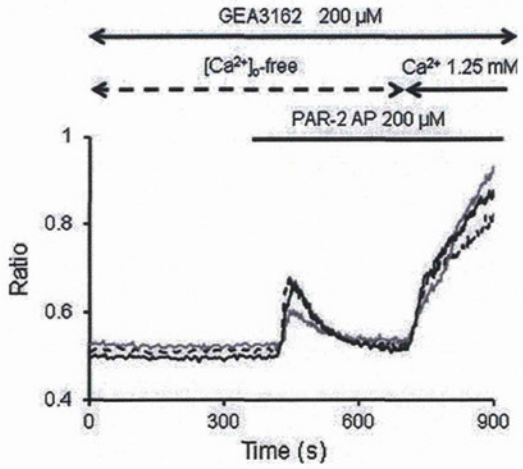

Fig. 9 Effects of GEA3162 on PAR2-AP-induced Ca^{2+} release and Ca^{2+} entry in lacrimal gland acinar cells. Cells were incubated in nominally Ca^{2+}-free Hepes buffer ($[Ca^{2+}]_o$-free) in the absence and presence of GEA3162 (200 μM) for 6 min, before the addition of PAR2-AP (200 μM). Ca^{2+} (1.25 mM) was reintroduced at 720 s. The temporal changes of $[Ca^{2+}]_i$ for three ROIs are depicted (*black*, *gray*, and *dotted lines*)

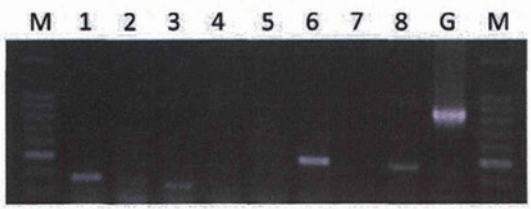

Lane	1	2	3	4	5	6	7	8
Intensity of bands	TRPC 1	TRPC 2	TRPC 3	TRPC 4	TRPC 5	TRPC 6	TRPC 7	TRPV 1
	++	-	+	-	-	+++	-	+

Fig. 10 RT-PCR analysis of TRPC and TRPV1 mRNAs in rat lacrimal gland acinar cells. Amplified PAR mRNA fragments obtained using RT-PCR were analyzed by ethidium-bromide agarose gel electrophoresis. +++, very strong band on the agarose gel; ++, strong and clearly visible band; +, weak band; (+), barely visible band; and −, band not visible. *G* GAPDH (positive control), *M* molecular standards

PAR2-induced Ca^{2+} mobilization mechanisms in lacrimal glands

The present study demonstrated that Ca^{2+} mobilization from intracellular Ca^{2+} stores was induced by PAR2-AP, suggesting the presence of metabotropic receptors that are activated by PAR2. Recently, Nishikawa et al. (2005) showed that the PAR2-AP SLIGRL-NH_2 has been reported to express PAR2 and causes tear secretion, most likely via PAR2 and that a PAR2-inactive peptide triggers tear secretion by stimulating parasympathetic nerves via an unidentified target molecule. Our finding confirmed that lacrimal glands express PAR2. PARs are GPCRs, and in general, changes in $[Ca^{2+}]_i$ upon GPCR activation are thought to be due to IP_3-mediated Ca^{2+} mobilization from an internal store, such as the sarco/endoplasmic reticulum (Berridge 2009). Most previous studies have reported that the activation of PAR2 leads to increases in intracellular calcium via a signal transduction mechanism that involves activation of PLC and the production of IP_3 (Böhm et al. 1996; Garrido et al. 2002; Wang et al. 2010). However, PAR2-mediated $[Ca^{2+}]_i$ changes were not inhibited by xestospongins and U73122 in exocrine cells, which is consistent with the lack of involvement of IP_3 in PAR2-mediated $[Ca^{2+}]_i$ changes in acinar cells of lacrimal glands. The lack of inhibition of trypsin- or PAR2-AP-induced responses by PLC and IP_3 receptors indicated that PAR2-mediated $[Ca^{2+}]_i$ changes were mainly IP_3-independent. There are a variety of Ca^{2+}-mobilizing second messenger systems in addition to IP_3, such as Ca^{2+} itself, which act through a process of Ca^{2+}-induced Ca^{2+} release, nicotinic acid adenine dinucleotide phosphate signaling, or cyclic ADP-ribose signaling. Moreover, we suggest that PAR2 stimulates a predominantly IP_3-independent Ca^{2+} mobilization pathway. These results are consistent with our previous data (Miura et al. 2011). However, it is important to note that PAR2 reactions may differ between species or tissues. In summary, PAR2-mediated responses in various cells appear to be IP_3-independent, although the exact mechanism through which Ca^{2+} is mobilized remains to be elucidated.

Receptor-specific regulation of CCE and NCCE

Based on the results of Ca^{2+} influx from extracellular spaces after stimulation with PAR2-AP, it was concluded that acinar cells express both CCE and NCCE. The increase in $[Ca^{2+}]_i$ evoked by CCE was partially decreased by calyculin A, low concentrations of Gd^{3+} and 2-APB (Fig. 8b, c). In addition, the production of NO then directly activates NCCE, and via activation of soluble guanylyl cyclase and PKG, NO also inhibits CCE (Moneer et al. 2003). Here, our data appeared to be consistent with these previous studies, and we suggest that PAR2 can reciprocally regulate CCE and NCCE via NO.

A similar situation exists in sympathetic neurons, where muscarinic and bradykinin receptors are each coupled to PLC and can activate TRPC6 via diacylglycerol, but only bradykinin (via IP_3-mediated depletion of intracellular stores) activates TRPC1 (Delmas et al. 2002). Two receptors (V1A and 5-HT2A), each using PLC to evoke a Ca^{2+} signals, have very different effects on Ca^{2+} entry (Moneer et al. 2003). These previous studies suggest that different receptors differentially regulate CCE and NCCE, but why should lacrimal glands differ in whether PAR2 reciprocally regulates the two pathways? Others (Moneer

and Taylor 2002; Brueggemann et al. 2005) have reported that AVP does not inhibit CCE in all A7r5 cell lines, and neither do all cell lines show activation of NCCE by AVP (Broad et al. 1999; Moneer and Taylor 2002; Dyer et al. 2005). These features were originally found in only a minority, including lacrimal glands, but they have become more common in cells from different sources. Our current data are consistent with above results and the results of our previous study (Miura et al. 2011). Thus, we suggest that PAR2-AP-evoked NCCE is dominant over CCE.

2-APB was originally introduced as a membrane-permeable inhibitor of IP_3 receptors (Maruyama et al. 1997) and has since been widely used to examine the functions of these receptors and the functions of other Ca^{2+} signaling mechanisms such as store-operated Ca^{2+} entry (Bootman et al. 2002). Certain TRPC channels (TRPC1, TRPC3, TRPC5 and TRPC6) have been reported to be inhibited by 2-APB (Ma et al. 2000; Delmas et al. 2002; Hu et al. 2004; Xu et al. 2005). In contrast, some TRPV channels (TRPV1, TRPV2 and TRPV3) are known to be activated by 2-APB (Chung et al. 2004; Hu et al. 2004). In our 2-APB experiments, PAR2-induced Ca^{2+} entry was almost completely inhibited in the presence of 2-APB. From our PCR analysis of RNA isolated from cells, TRPC1, -3 and -6 were expressed (Fig. 10). Our data are consistent with these previous studies. Moneer et al. (2005) showed that almost 90 % of TRPC expressed in A7r5 cells is TRPC1, whereas cells in which AVP stimulates NCCE and inhibits CCE express a more balanced mixture of the major TRPC subtypes: 35 % TRPC1, 35 % TRPC6, 16 % TRPC2, and 7 %TRPC3. They suggest that these cells are perhaps more likely to express hetero-oligomeric TRPC channels (Clapham et al. 2001). Our data are similar to above data, with the exception of TRPC2. It is noteworthy that, in other cells, a change in the expression of a single TRPC protein has been reported to change the properties of both CCE and NCCE pathways, suggesting that the different channels may share some TRPC subunits. In HEK-293 cells, for example, overexpression of TRPC3 does not increase the amplitude of CCE, yet it both modifies its behavior by suppressing its sensitivity to Gd^{3+}, NO, and mitochondrial uncouplers and increases receptor-regulated Ca^{2+} entry via NCCE (Zhu et al. 1998; Thyagarajan et al. 2001). In DT40 cells, TRPC3 can also modulate the behavior of endogenous CCE and contribute to NCCE (Putney 2004). Thus, we suggest that TRPC1 interacts with CCE and NCCE, and that both TRPC3 and -6 interact with NCCE. Therefore, hetero-oligomers of TRPC proteins may contribute to the formation of both CCE and NCCE in lacrimal gland acinar cells, and the composition of the channel may determine its susceptibility to inhibition by PKG (for CCE) and activation by NO (for NCCE).

Recent studies indicated that TRPV1 receptor increased secretion of submandibular gland (Zhang et al. 2010), and that PAR2 regulates TRPV1 to induce hyperalgesia and sensitize TRPV1 by PKC in HEK 293 cell (Amadesi et al. 2006). Consistently, our PCR analysis showed expression of TRPV1 in lacrimal glands. TRPV1 can play a role in PAR2 activation-induced $[Ca^{2+}]_i$ dynamics in the lacrimal gland, although further experiments will be necessary to completely clarify the relationship between CCE/NCCE and TRPV1 receptors in the lacrimal gland.

Based on the results of Ca^{2+} influx from extracellular spaces after stimulation with PAR2-AP, it was concluded that acinar cells express CCE and NCCE. Further experiments will be necessary to completely clarify the relationship between CCE and NCCE with respect to PAR2 in the lacrimal gland. Regardless of the lack of details of the intracellular signaling systems, we can conclude that exocrine cells possess redundant mechanisms to maintain secretion at a certain functional level.

Acknowledgments We wish to express our thanks to Mr. M. Hirakawa, Department of Anatomy, for his technical assistance. This work was supported by research grants from the Ministry of Education, Culture, and Science of Japan (K.K.; 23592585) and from the Promotion and Mutual Aid Corporation for Private Schools of Japan. Some of this work was performed at the Advanced Medical Science Center of Iwate Medical University, which also provided financial support.

References

Amadesi S, Cottrell GS, Divino L, Chapman K, Grady EF, Bautista F, Karanjia R, Barajas-Lopez C, Vanner S, Vergnolle N, Bunnett NW (2006) Protease-activated receptor 2 sensitizes TRPV1 by protein kinase Cepsilon- and A-dependent mechanisms in rats and mice. J Physiol 575:555–571

Berridge MJ (2009) Inositol trisphosphate and calcium signalling mechanisms. Biochim Biophys Acta 1793:933–940

Birnbaumer L, Yildirim E, Abramowitz J (2003) A comparison of the genes coding for canonical TRP channels and their M, V and P relatives. Cell Calcium 33:419–432

Böhm SK, Kong W, Bromme D, Smeekens SP, Anderson DC, Connolly A, Kahn M, Nelken NA, Coughlin SR, Payan DG, Bunnett NW (1996) Molecular cloning, expression and potential functions of the human proteinase-activated receptor-2. Biochem J 314:1009–1016

Bootman MD, Collins TJ, Mackenzie L, Roderick HL, Berridge MJ, Peppiatt CM (2002) 2-aminoethoxydiphenyl borate (2-APB) is a reliable blocker of store-operated Ca2 +entry but an inconsistent inhibitor of InsP3-induced Ca2+ release. FASEB J 16:1145–1150

Broad LM, Cannon TR, Taylor CW (1999) A non-capacitative pathway activated by arachidonic acid is the major Ca2+ entry mechanism in rat A7r5 smooth muscle cells stimulated with low concentrations of vasopressin. J Physiol 517:121–134

Brueggemann LI, Markun DR, Barakat JA, Chen H, ByronK L (2005) Evidence against reciprocal regulation of Ca2+ entry by vasopressin in A7r5 aortic smooth muscle cells. Biochem J 388:237–244

Camerer E, Huang W, Coughlin SR (2000) Tissue factor- and factor X-dependent activation of protease-activated receptor 2 by factor VIIa. Proc Natl Acad Sci U S A 97:5225–5260

Cheng KT, Liu X, Ong HL, Ambudkar IS (2008) Functional requirement for Orai1 in store-operated TRPC1–STIM1 channels. J Biol Chem 283:12935–12940

Chung MK, Lee H, Mizuno A, Suzuki M, Caterina MJ (2004) TRPV3 and TRPV4 mediate warmth-evoked currents in primary mouse keratinocytes. J Biol Chem 279:21569–21575

Clapham DE, Runnels LW, Strübing C (2001) The TRP ion channel family. Nat Rev Neurosci 2:387–396

Cocks TM, Moffatt JD (2000) Protease-activated receptors: sentries for inflammation? Trends Pharmacol Sci 21:103–108

Coughlin SR (2000) Thrombin signaling and protease-activated receptors. Nature 407:258–264

Dartt DA (1994) Regulation of tear secretion. Adv Exp Med Biol 350:1–9

Dartt DA (2009) Neural regulation of lacrimal gland secretory processes: relevance in dry eye diseases. Prog Retin Eye Res 28:155–177

Delmas P, Wanaverbecq N, Abogadie FC, Mistry M, Brown DA (2002) Signaling microdomains define the specificity of receptor-mediated InsP3 pathways in neurons. Neuron 34:209–220

Déry O, Corvera CU, Steinhoff M, Bunnett NW (1998) Proteinase-activated receptors: novel mechanisms of signaling by serine proteases. Am J Physiol 274:C1429–C1452

Dyer JL, Liu Y, Pino de la Huerga I, Taylor CW (2005) Long-lasting inhibition of adenylyl cyclase selectively mediated by inositol 1,4,5-trisphosphate-evoked calcium release. J Biol Chem 280:8936–8944

Garrido R, Segura B, Zhang W, Mulholland M (2002) Presence of functionally active protease-activated receptors 1 and 2 in myenteric glia. J Neurochem 83:556–564

Gromada J, Jørgensen TD, Dissing S (1995) The release of intracellular Ca2 + in lacrimal acinar cells by a-, b-adrenergic and muscarinic cholinergic stimulation: the roles of inositol triphosphate and cyclic ADP-ribose. Pflügers Arch 429:751–756

Hirano K, Kanaide H (2003) Role of protease-activated receptors in the vascular system. J Atheroscler Thromb 10:211–225

Hodges RR, Dartt DA (2003) Regulatory pathways in lacrimal gland epithelium. Int Rev Cytol 231:129–196

Hollenberg MD (1999) Protease-activated receptors: PAR-4 and counting: how long is the course. Trends Pharmacol Sci 20:271–273

Hu HZ, Gu Q, Wang C, Colton CK, Tang J, Kinoshita-Kawada M, Lee LY, Wood JD, Zhu MX (2004) 2-aminoethoxydiphenyl borate is a common activator of TRPV1, TRPV2, and TRPV3. J Biol Chem 279:35741–35748

Ishihara H, Connolly AJ, Zeng D, Kahn ML, Zheng YW, Timmons C, Tram T, Coughlin SR (1997) Protease-activated receptor 3 is a second thrombin receptor in humans. Nature 386:502–506

Jardin I, Redondo PC, Salido GM, Rosado JA (2008) Phosphatidylinositol 4,5-bisphosphate enhances store-operated calcium entry through hTRPC6 channel in human platelets. Biochim Biophys Acta 1783:84–97

Kahn ML, Zheng YW, Huang W, Bigornia V, Zeng D, Moff S, Farese RV Jr, Tam C, Coughlin SR (1998) A dual thrombin receptor system for platelet activation. Nature 394:690–694

Kamada Y, Saino T, Oikawa M, Kurosaka D, Satoh Y (2012) P2Y purinoceptors induce intra- cellular calcium dynamics of acinar cells in rat lacrimal glands. Histochem Cell Biol 137:97–106

Kawabata A, Kuroda R (2000) Protease-activated receptor (PAR), a novel family of G protein-coupled seven trans-membrane domain receptors: activation mechanisms and physiological roles. Jpn J Pharmacol 82:171–174

Kawabata A, Kuroda R, Minami T, Kataoka K, Taneda M (1998) Increased vascular permeability by a specific agonist of protease-activated receptor-2 in rat hindpaw. Br J Pharmacol 125: 419–422

Kawabata A, Morimoto N, Nishikawa H, Kuroda R, Oda Y, Kakehi K (2000a) Activation of protease-activated receptor-2 triggers mucin secretion in the rat sublingual gland. Biochem Biophys Res Commun 270:298–302

Kawabata A, Nishikawa H, Kuroda R, Kawai K, Hollenberg MD (2000b) Proteinase-activated receptor-2 (PAR-2): regulation of salivary and pancreatic exocrine secretion in vivo in rats and mice. Br J Pharmacol 129:1808–1814

Kawabata A, Kuroda R, Morimoto N, Kawao N, Masuko T, Kakehi K (2001) Lipopolysaccharide-induced subsensitivity of protease-activated receptor-2 in the mouse salivary glands in vivo. Naunyn Schmiedebergs Arch Pharmacol 364:281–284

Kawabata A, Kuroda R, Nishida M, Nagata N, Sakaguchi Y, Kawao N, Nishikawa H, Arizono N, Kawai K (2002) Protease-activated receptor-2 (PAR-2) in the pancreas and parotid gland: immunolocalization and involvement of nitric oxide in the evoked amylase secretion. Life Sci 71:2435–2446

Liao Y, Erxleben C, Abramowitz J, Flockerzi V, Zhu MX, Armstrong DL, Birnbaumer L (2008) Functional interactions among Orai1, TRPCs, and STIM1 suggest a STIM-regulated heteromeric Orai/TRPC model for SOCE/Icrac channels. Proc Natl Acad Sci USA 105:2895–2900

Linley JE, Rose K, Patil M, Robertson B, Akopian AN, Gamper N (2008) Inhibition of M current in sensory neurons by exogenous proteases: a signaling pathway mediating inflammatory nociception. J Neurosci 28:11240–11249

Looms DK, Tritsaris K, Nauntofte B, Dissing S (2001) Nitric oxide and cGMP activate Ca2+-release processes in rat parotid acinar cells. Biochem J 355:87–95

Ma HT, Patterson RL, van Rossum DB, Birnbaumer L, Mikoshiba K, Gill DL (2000) Requirement of the inositol trisphosphate receptor for activation of store-operated Ca2+ channels. Science 287:1647–1651

Macfarlane SR, Seatter MJ, Kanke T, Hunter GD, Plevin R (2001) Proteinase-activated receptors. Pharmacol Rev 53:245–282

Maruyama T, Kanaji T, Nakade S, Kanno T, Mikoshiba K (1997) 2APB, 2-aminoethoxydiphenyl borate, a membrane-penetrable modulator of Ins(1,4,5)P3-induced Ca2+ release. J Biochem (Tokyo) 122:498–505

Matsuoka H, Harada K, Ikeda T, Uetsuki K, Sata T, Warashina A, Inoue M (2009) Ca2 + pathway involved in the refilling of store sites in rat adrenal medullary cells. Am J Physiol Cell Physiol 296:C889–C899

Miura H, Saino T, Sato M, Satoh Y (2011) Role of protease activated receptors in intracellular calcium dynamics of neurons and satellite cells in rat superior cervical ganglia. Bioimages 19:17–27

Moneer Z, Taylor CW (2002) Reciprocal regulation of capacitative and non-capacitative Ca2 + entry in A7r5 vascular smooth muscle cells: only the latter operates during receptor activation. Biochem J 362:13–21

Moneer Z, Dyer JL, Taylor CW (2003) Nitric oxide co-ordinates the activities of the capacitative and non-capacitative Ca2+-entry pathways regulated by vasopressin. Biochem J 370:439–448

Moneer Z, Pino I, Taylor EJ, Broad LM, Liu Y, Tovey SC, Staali L, Taylor CW (2005) Different phospholipase-C-coupled receptors differentially regulate capacitative and non-capacitative Ca2+ entry in A7r5 cells. Biochem J 389:821–829

Montell C (2003) The venerable inveterate invertebrate TRP channels. Cell Calcium 33:409–417

Nguyen TD, Moody MW, Steinhoff M, Okolo C, Koh D-S, Bunnett NW (1999) Trypsin activates pancreatic duct epithelial cell ion channels. J Clin Invest 103:261–269

Nishikawa H, Kawai K, Tanaka M, Ohtani H, Tanaka S, Kitagawa C, Nishida M, Abe T, Araki H, Kawabata A (2005) Protease-